Materials Today Physics 27 (2022) 100805

Contents lists available at ScienceDirect

Materials Today Physics

journal homepage: www.journals.elsevier.com/materials-today-physics

Density functional thermodynamic description of spin, phonon and displacement degrees of freedom in antiferromagnetic-to-paramagnetic phase transition in $YNiO_3$

J.L. Du [a,b], O.I. Malyi [c], S.-L. Shang [b], Y. Wang [b], X.-G. Zhao [c], F. Liu [a], A. Zunger [c], Z.-K. Liu [b,*]

[a] State Key Laboratory of Solidification Processing, Northwestern Polytechnical University, Xi'an, Shaanxi 710072, China
[b] Department of Materials Science and Engineering, The Pennsylvania State University, University Park, PA, 16802, USA
[c] Renewable and Sustainable Energy Institute, University of Colorado, Boulder, CO, 80309, USA

A B S T R A C T

This work demonstrates a direct density functional description of the finite-temperature thermodynamic properties of solids exhibiting phase transitions through positional and spin symmetry breaking degrees of freedom. A classic example addressed here is the rare-earth (R) nickelates $RNiO_3$ where the ground state is characterized by crystallographic and magnetic (e.g., antiferromagnetic) long-range order (LRO), whereas the higher temperature paramagnetic phase manifests a range of local spin and positional symmetry breaking motifs with short-range order (SRO). Unlike time-dependent simulations of spin and positional degrees of freedom, in the present work, phases are described via a superposition of static configurations constructed by populating a periodic base lattice supercell allowing for the formation of energy lowing distribution of positional and spin local motifs. The thermal populations of the configurations in such a superposition phase are obtained from the energy-minimized Density Functional Theory (DFT)-calculated partition functions at different temperatures. This approach offers flexible inclusion of different physical contributions to the free energy, such as elastic, electronic and phonon free energies, all obtained from the same underlying DFT total energy calculations of periodic structures. The thermodynamic and magnetic properties of both LRO and SRO crystallographic and spin phases, including antiferromagnetic (AFM) to paramagnetic (PM) Néel phase transition in $YNiO_3$ are studied. Including spin and phonon contributions, we find a DFT-calculated Néel temperature to be 144 K in satisfactory agreement with the experimental value of 145 K; whereas omitting the phonon contribution, one obtains a Néel temperature of 81 K. We present phonon contributions to the DFT-calculated temperature-dependent SRO, heat capacities, and the polymorphous distribution of nonzero local magnetic moments in the PM phase. This approach thus extends to finite temperatures the symmetry-broken DFT description of both the AFM and PM phases, demonstrating that a thermodynamic superposition approach based on symmetry broken configurations evaluated by a mean-field like DFT is sufficient to obtain a consistent description of the thermal physics of the AFM, PM phases and their interconversion in 3d oxides illustrated by $YNiO_3$.

1. Introduction

The current work addresses the calculations of finite-temperature thermodynamic properties of crystalline solids exhibiting phase transitions through the combination of multiple microscopic degrees of freedom such as spin, phonon, and ionic displacement. We explain the concept by first discussing how multiple degrees of freedom often necessitate considerations of larger than usual unit cell sizes affording a distribution of different local motifs even before the temperature is considered. Theoretical predictions of crystallographically *long-range ordered ground state* structures [1–6] are often conducted by considering simple structures made of just one or very few structural motifs, leading to the smallest possible fundamental unit cells. In contrast, other non-ground state structures of the same system, such as paraelastic, paramagnetic, or paraelectric phases, could manifest a distribution of numerous local positional, spin, or dipole motifs with a combination of both long-range order (LRO) and short-range order (SRO), which would require the large-than-minimal cell to achieve a correct crystallographic description. Perhaps the best-known examples of the 'spatially fluctuating' (or polymorphous) phases are two component substitutional chemical alloys $(AC)_x(BC)_{1-x}$ of composition x, where the alloy phase can consist of a distribution of many different C atoms coordinated locally at different lattice sites by a different number (n,m) of A and B neighbors A_nB_m [6]. Interestingly, such inherently large unit cell phases manifesting a polymorphous distribution of local motifs can also exist in pure, non-alloyed systems [7–11]. The microscopic degrees of freedom (*m*-DOF) building such local motifs can be local *positional motifs* (such as differently tilted octahedra in perovskites [12–14]), or local configurations of *magnetic moment motifs* (as in paramagnetic phases [7,9]), or local *dipole motifs* (as in paraelectric phases [14]). Such local motifs can

* Corresponding author.
E-mail address: prof.zikui.liu@psu.edu (Z.-K. Liu).

https://doi.org/10.1016/j.mtphys.2022.100805
Received 18 May 2022; Received in revised form 26 July 2022; Accepted 28 July 2022
Available online 5 August 2022

be calculated via the minimization of the internal energy E_0, as in Jahn-Teller distortions in manganates [10], or structural disproportionation of octahedra in nickelates [11], or due to lone-pair-induced positional distortions as in Pb or Bi salts [15]—all representing *intrinsic* symmetry breaking. In the same way that large unit cells that occur naturally in chemically disordered $(AC)_x(BC)_{1-x}$ alloys were often approximated by a 'virtual crystal' averaged cell, para phases of pure, non-alloyed systems were also often treated theoretically using averaged, high symmetry cells. When used as 'input' to electronic structure calculations, such a drastic approximation of replacing a polymorphous cell by its high symmetry virtual average led to severe contradiction with the experiment, as illustrated in Refs. [7,10].

The current approach avoids such averaging by considering the full distribution of local motifs instead. By exploring energy minimization due to such intrinsic symmetry breaking while avoiding the restriction of minimal size, high symmetry, 'average' unit cells [16], it was recently pointed out that paramagnetic phases of oxide Mott insulators can become naturally insulating, as opposed to the more traditional 'false metal' predictions [17]. While the emergence of symmetry-breaking modes does not necessarily require temperature for their formation, as temperature increases, such distortions can be further amplified and modify their distributions [16].

In the present paper, we extend such DFT descriptions based on the intrinsic internal energy, E_0, of large unit cell configurations to finite temperature, where the free energy E_0-TS is the central quantity. We do so without using the usual time-dependent simulations, such as molecular dynamics. Instead, the polymorphous/fluctuating phases are described via a superposition of static configurations constructed by decorating a base lattice supercell with local, symmetry broken positional, and spin motifs. We study the electronic properties of both LRO and SRO crystallographic and magnetic phases, including antiferromagnetic (AFM) to paramagnetic (PM) phase transition in $YNiO_3$. This approach incorporates electronic and phonon contributions to the DFT-calculated temperature-dependent SRO, heat capacities, the polymorphous distribution of nonzero local magnetic moments in the PM phase, and the predicted Néel temperature.

1.1. The present first-principles thermodynamic approach in the context of other methods

We first describe alternative approaches to the problem not used in the present work.

Modeling fluctuating phases without temperature via *configurational approximants*: Sometimes, one wishes to focus on the electronic properties of disordered phases without explicitly describing temperature-induced dynamic fluctuations. Such are the temperature-independent configurational approximants to fluctuating phases. These include the virtual crystal approximation (VCA) [18,19], the coherent potential approximation (CPA) [20–22], and the special quasi-random structures (SQS) containing the polymorphous distributions of local motifs [23]. In these approaches, one constructs a static structural approximant for a high-temperature disorder, modeling its electronic properties by applying DFT to such a static approximant.

Modeling temperature-induced disorder by dynamic model Hamiltonian simulations: More generally, one may wish to describe the electronic properties of spatially fluctuating phases as an explicit function of temperature. Indeed, the description of the nature of such polymorphous phases is one of the main challenges in contemporary electronic structure theories, which is why it is being addressed in the current paper. The standard quantum mechanical description of high temperature, spatially fluctuating phases is often based on model Hamiltonians that provide the energy of a given configuration in terms of the microscopic degrees of freedom. These degrees of freedom could be (a) displacements, (b) magnetic moments, or (c) electric dipoles. Hamiltonians of types (a)-(c) are then simulated via statistical approaches such as Monte-Carlo sampling, providing the different phases as a function of temperature. Examples follow:

a) *When the microscopic degrees of freedom are defined by local occupation of lattice sites of particular (say, A or B) atoms*: one often uses the generalized Ising Hamiltonian model [6]. It employs lattice configuration σ, and atom-atom interaction energies $\{J_f\}$ that can be evaluated from DFT calculations [24–26] of different periodic solids via the cluster expansion method [5,6,25,26]. Simulations of such Ising Hamiltonian via the Monte-Carlo method provide the T vs. x structural phase diagram, phase transition temperatures, as well as SRO and LRO vs. temperature. Examples include the phase diagram of various alloys [27–29] calculated in such a manner.
b) *When the microscopic degrees of freedom are defined by local spins and the ensuing magnetic moments*, one often uses the representation of the Heisenberg Hamiltonian. In this case, the spin-spin exchange interactions are obtained from DFT via using the linear response method [30] as an example. Monte-Carlo simulations of this Hamiltonian provide a description of the low-temperature spin ground state as well as the Néel transition temperature to the PM phase. Examples include such modeling of the AFM-to-PM Néel transition in GaMnAs as well as $Bi_{1-x}Sb_x$ [31–34].
c) *When the microscopic degrees of freedom are defined by the local ferroelectric dipole*, the model Hamiltonian is often fitted from DFT static and displacement calculations [35–37]. The corresponding Hamiltonian is solved via Monte-Carlo [35] to give ferroelectric-paraelectric (FE-PE) phases. Examples include the FE-PE phases of $BaTiO_3$ and $BiFeO_3$ [35,36].

The above Hamiltonian models (a)-(c) can utilize first-principles inputs, where the interaction energies are fit to the DFT data. However, the underlying Hamiltonian used to fit such interactions involves truncation to certain interaction types (such as pairs only) or ranges (such as nearest and next nearest neighbors). Furthermore, coupling between different types of m-DOF's, such as spins and lattice distortion, are not included automatically but can be accommodated as additional, specialized terms in the Hamiltonian that will require additional fits. For these reasons, we chose here to avoid such model Hamiltonian simulations.

1.2. The superposition approach

Alternative approaches to the theory of finite temperature, spatially fluctuating phases are based on the *superposition of periodic configurations* $\{\sigma\}$ created by populating a base lattice with local motifs, such as A/B atomic species, spin, octahedral tilting, etc. This approach extends density functional applications to finite temperature, does not require the decomposition of DFT total energies into individual interactions as in the model Hamiltonian, and does not involve a time scale. The superposition approach also allows flexible inclusion of different physical contributions into the free energy, such as phonon free energies, elastic energies or electronic entropy, all evaluated directly by DFT. Next, the essential pertinent ideas of the superposition approach are summarized.

The superposition approach shares common elements with the cluster expansion theory [5,26,38] and with basic free energy expansions in thermodynamics [39]. In the cluster expansion theory [5,25,26], the total excess energy, ΔE, of atomic configuration σ is given as a combination of the interaction energies J_f of "figures" f (= pairs, three bodies, etc.) weighted by the D_f (degeneracy of figure f) and by the occurrence Π_f of a figure f in configuration σ,

$$\Delta E(\sigma) = \sum_f D_f \Pi_f(\sigma) J_f. \tag{1}$$

Inversion of this equation provides the interaction energy J_f as a weighted sum of DFT total energies of a set of periodic structure (s),

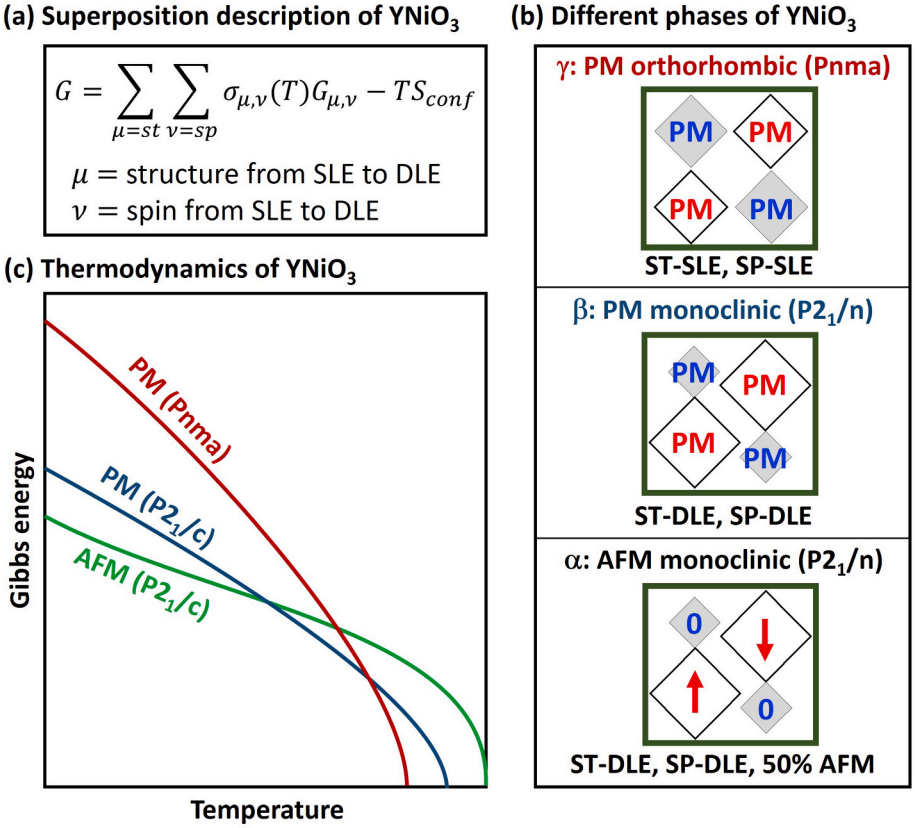

Fig. 1. Summary of thermodynamic data on $YNiO_3$ and different degrees of freedom known in $YNiO_3$. (a) Basic idea of superposition of SP and ST for a description of thermodynamics of fluctuating phases, where the Gibbs energy of the system at finite temperature equals the weighted summation of free energy of each configuration plus the configurational entropy among the configurations. (b) Definition of the three phases indicating spin disproportionation and bond disproportionation. Summary on different types of $YNiO_3$ phases reported in the literature and SP and ST degrees of freedom. (c) Schematic illustration of temperature-dependent Gibbs energies of different $YNiO_3$ phases.

$$J_f = \frac{1}{ND_f}\sum_s^n [\Pi_f(s)]^{-1}\Delta E(s). \quad (2)$$

Resubstituting these interaction energies {J_f} in Eq. (1) shows *that the excess energy of any arbitrary configuration σ' can be expressed as a superposition of the total energies of a set of the other configurations (s),*

$$\Delta E(\sigma') = \sum_s \xi_s(\sigma')\Delta E(s) \quad (3)$$

with coefficients given by,

$$\xi_n(\sigma) = \sum_g [\Pi_g(\sigma)]^{-1}[\Pi_g(\sigma)]. \quad (4)$$

Equations (3) and (4) [38] define the superposition concept for the simple case of total lattice energies at $T = 0$ K, and show that it requires examining the convergence with respect to the number of configurations included in the superposition expansion. We next discuss the generalization to the thermodynamic limit.

1.3. *The superposition approach based on finite-temperature thermodynamics*

This approach replaces the total energy at $T = 0$ K noted in Eqs. (1)–(4) by the free energy of different configurations at finite temperature. Using a canonical ensemble of phase, denoting both crystal space group with unit cell composed of N atoms and the magnetic symmetry at given volume V and temperature T, the total partition function of the superposition state $Z(V,T)$ can be written as the sum over the partition function of individual configurations, i.e.,

$$Z(V,T) = \sum_\sigma \omega_\sigma Z_\sigma(V,T) \quad (5)$$

where σ represents a specific configuration distinguished by a different occupation of lattice sites by microscopic degrees of freedom (displacements, spins, dipoles). In Eq. (5), ω_σ is the degeneracy factor representing the multiplicity of configuration σ determined by the symmetry of the selected lattice. $Z_\sigma(V,T)$ is the partition function of configuration σ expressed by [39],

$$Z_\sigma(V,T) = \exp[-F_\sigma(V,T)/k_BT] \quad (6)$$

where k_B represents the Boltzmann's constant and $F_\sigma(V,T)$ is the Helmholtz energy of configuration σ as discussed in the next section.

The main advantages of the finite temperature superposition approach to spatially fluctuating phases are that (i) the existence of spatially fluctuating components in a para phase is explicitly included as a superposition without using a time domain as in dynamic simulations. (ii) The energetics are obtained from first-principles DFT without requiring the step of resolving DFT total energies into elementary interactions, such as effective cluster interactions, then truncating, as in the cluster expansion method [24,25] or the Heisenberg Hamiltonian [30,35,36]. (iii) One can readily include the interaction between the various microscopic degrees of freedom, such as electronic structure physics included in DFT, along with phonon physics, calculated from the same supercell in DFT, allowing electron-phonon coupling. Another interesting advantage is that (iv) once one computes the probability or thermal populations x_σ of the different configurations, it is possible to use them for describing other thermodynamic observables of the superposition phase. Within this framework, the property Pr of the superposition phase is connected to the respective properties $Pr_{\sigma j}$ of the individual configurations [40,41], such as band gaps or short-range order, i.e.,

$$Pr(x,T) = J_0 + \sum_{j=0}^{J} x_{\sigma j}(x,T)Pr_{\sigma j} \quad (7)$$

where the additional term J_0 is introduced by the partition function due to mixing of multiple configurations, and it exists for properties such as

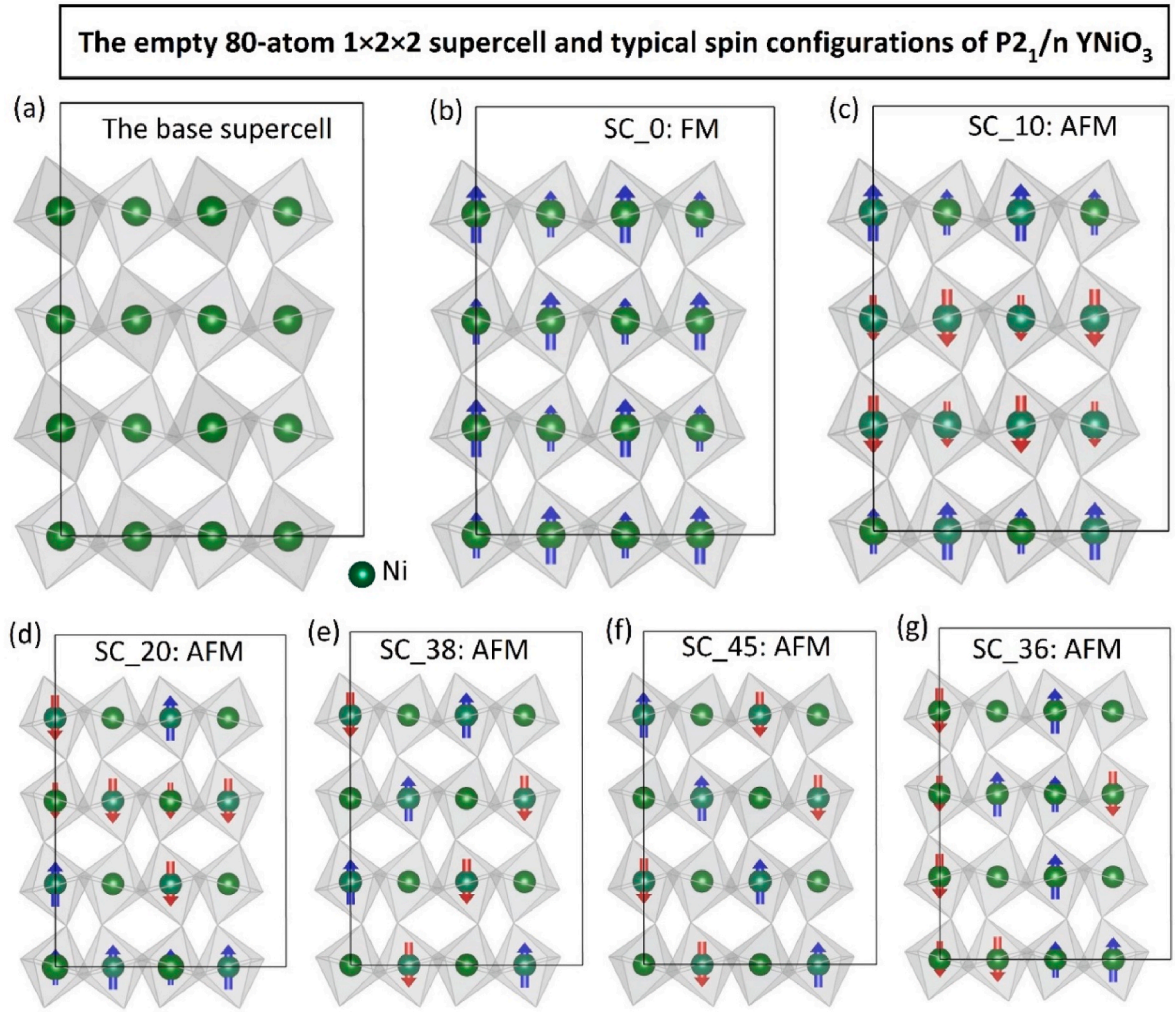

Fig. 2. Schematic illustration of representative spin configurations (SC) considered in this work. (a) The empty 80-atom 1×2×2 supercell with 16 Ni sites (16 Ni-centered oxygen octahedra) of the monoclinic $P2_1/n$ $YNiO_3$ phase, where each Ni atom is represented by a green sphere. (b–g) The typical spin configurations in the 80-atom 1×2×2 supercell (with SC_45 being the spin ground state AFM configuration) of the monoclinic $P2_1/n$ $YNiO_3$ phase. The zero-spin, spin up, and spin down Ni atoms forming the oxygen octahedra are denoted by no-arrows, upward-blue arrows, and downward-red arrows, respectively. Relative length of arrows represents the magnitude of the magnetic moment. The Y and O atoms are not displayed for clarity. (For interpretation of the references to colour in this figure legend, the reader is referred to the Web version of this article.)

entropy, heat capacity, and bulk modulus as shown later in Eqs. (12), (13) and (15) of Section III B.

In the present work, we illustrate the finite-temperature superposition method (Fig. 1) to study the magnetic transition between AFM and PM in yttrium nickelate ($YNiO_3$) within the monoclinic $P2_1/n$ space group. The $RNiO_3$ family of nickelates [42–50] exhibits the octahedral volume disproportionation effect, and spin disproportionation effects. The phase transitions in $RNiO_3$ family were previously investigated by using a combination of density functional theory and dynamical mean-field theory calculations [51–54], where the critical role of strong correlation was emphasized. Interestingly, by allowing mean-field DFT symmetry-breaking energy lowering in large supercells [55], it was demonstrated that the trend of the band gaps, magnetic moments, ground state symmetry, ligand hole effects, and structural deformation modes, including Jahn-Teller distortions in AFM and PM phases in ABO_3 perovskites could be described without requiring strong correlation. In the present work, we extend the method to finite temperature effects using the DFT-based superposition approach [39].

2. The superposition method for magnetic phases in $YNiO_3$: combining spin and structural degrees of freedom

2.1. The different degrees of freedom and their representation as a superposition of configuration

The phase diagram of $YNiO_3$ features three phases [44–49]: (a) a spin-ordered AFM structurally monoclinic $P2_1/n$ insulator phase, α, existing at low temperature, transitioning at the Néel temperature (T_N = 145 K) to the (b) spin-disordered PM structurally monoclinic $P2_1/n$ insulator phase, β, that transitions to the (c) spin-disordered PM structurally orthorhombic Pbnm metallic phase, γ, at the metal-to-insulator transition temperature (T_{MI} = 582 K). More specifically, by "spin-disordered PM" we mean that the para phases lack LRO but can have correlated-disorder and SRO. Each of these phases α, β, and γ has both spin (SP) and structural (ST) degrees of freedom, as illustrated in Fig. 1. Both α and β phases have two *structural* local environments, called 'Double Local Environment' (DLE), whereby there are two types of Ni–O octahedra with different volumes, one small and the other large. These phases also have two types of *spin* local environments: in phase α, these are ~1.1 μ_B/atom spin (up and down) and the zero spin sublattices,

whereas in the phase β the two local spin environments correspond to Ni sites with a distribution of magnetic moments between 0 and ~1.1 μ_B/atom. In contrast, the γ phase is believed to have a single type of local environment (SLE)-both for spin and structure, forcing the system to be metallic. The existence of such ST and SP degrees of freedom ranging between SLE and DLE suggests that an appropriate theoretical description of $YNiO_3$ phases requires explicate accounting of ST and SP motifs and their coupling.

Fig. 1 provides an overview of the superposition method as it pertains to $YNiO_3$, indicating the different degrees of freedom in each phase. Fig. 1(a) describes the basic superposition equation where the equilibrium phase at temperature T is a superposition over configurations, plus the entropy due to mixing the spatially fluctuating configurations. As the temperature is raised, the system is expected to exhibit a different superposition of configurations, thereby transitioning from phase α, β, and γ. Fig. 1(b) defines the three base phases showing two types of octahedra (small and large volume) and two types of spin arrangements. Computationally, each phase is described by a supercell with atomistically resolved positions and spins. Fig. 1(c) indicates the transitions expected vs. temperature.

2.2. Selection of base and enumerating spin and lattice configurations

Allowing for various levels of inclusion of spin and structural degrees of freedom leads to a number of possibilities for representations. Had the $YNiO_3$ phase been considered as nonmagnetic, its minimum cell would contain four ABO_3 formula units (f.u.), defined as a 20-atom unit cell, referred as base cell in the rest of the paper. A minimum base cell of 16 f.u.(16 Ni-centered octahedra) i.e., 80 atoms for the monoclinic $P2_1/n$ $YNiO_3$ is shown Fig. 2(a), There are 35 possible supercells in terms of the spatial arrangements of four 20-atom base cells. If one populates such an 80-atom supercell by restricting the initial spin configuration (i.e., prior to the self-consistent calculation) to be 8 Ni atoms with zero moments and 8 Ni atoms with nonzero moments, this creates 256 spin configurations for each supercell, of which 37 are symmetry independent (by considering the degeneracy factor through the symmetry analysis [56]) for the 80-atom 1×2×2 supercell. Based on the DFT total energy calculations, we found that the two inequivalent Ni sites in $P2_1/n$ $YNiO_3$ exhibit asymmetric magnetic moments, see Table AI; half of the Ni atoms in those low energy AFM configurations are nonmagnetic with zero spin moments, while the other half is magnetic with nonzero spin moments in accordance with the results reported in the literature [44,57]. Accordingly, the initial magnetic moment was set as zero for half Ni atoms in all spin configurations in the present work, see details in Appendix I. The corresponding local magnetic moments of Ni atoms in the 37 independent spin configurations after optimization are provided in Table AII, and their corresponding multiplicity is given in Table AIII of Appendix I. Typical spin configurations of the monoclinic $P2_1/n$ $YNiO_3$ are depicted in Fig. 2(b)–(g) for the 80-atom 1×2×2 supercell. It turns out that those low-energy states are the spin-ordering AFM configurations, where the ground state AFM configuration is featured by the spin ordering shown in Fig. 2(f).

The present work focuses on the 80-atom 1×2×2 supercell as the base model for the α and β *monoclinic* $P2_1/n$ $YNiO_3$ phases in Fig. 1 (extension to the orthorhombic γ phase is presently not considered). It is worthwhile to mention that in combination with the accurate energies determined from first-principles phonon calculations, the present superposition method can be extended to large magnetic systems via the cluster expansion method and/or the machine learning model to explore the system size effects. Unless specified otherwise, the discussions in the rest of the paper are for the α and β monoclinic $P2_1/n$ $YNiO_3$ phases, i.e., the spin-ordered AFM structurally monoclinic $P2_1/n$ insulator α phase and the spin-disordered PM structurally monoclinic $P2_1/n$ insulator β phase, see Fig. 1(b).

3. Execution of the thermodynamic superposition method

3.1. Entropy factor in the superposition method

Eqs. (5) and (6) are the basis of the superposition approach to the first-principles thermodynamics. Here, the physical content used by Eqs. (5) and (6) is explained as it applied to superposition. This section also details how the various thermodynamic quantities and the α-to-β Néel phase transitions are calculated.

The Helmholtz energy of a configuration in Eq. (6) is given by,

$$F_\sigma(V,T) = E_\sigma(V,T=0) + F_{\sigma,vib}(V,T) + F_{\sigma,\mathrm{ele}}(V,T) \tag{8}$$

where σ represents a specific configuration distinguished by a different occupation of lattice sites by microscopic degrees of freedom, $E_\sigma(V,T=0)$ is the 0 K total internal energy of configuration σ determined from periodic DFT calculations, and $F_{\sigma,vib}(V,T)$ is the lattice vibrational free energy of configuration σ. Here, $F_{\sigma,vib}(V,T)$ can be obtained either from (i) the DFT phonon calculations (details as described in Ref. [57]), or (ii) via the simplified Debye model [58]. The term $F_{\sigma,\mathrm{ele}}(V,T)$ is the thermal electronic contribution related to electron excitation at finite temperature [59]. For the insulating monoclinic $P2_1/n$ $YNiO_3$, it is negligible [57,60].

The superposition of the partition functions of the different configurations in Eq. (5) gives the total Helmholtz energy of the superposition phase as,

$$F(V,T) = -k_B T \ln Z(V,T) = \sum_\sigma x_\sigma F_\sigma(V,T) - TS_{conf}(V,T) \tag{9}$$

where the probability or thermal population of configuration σ is given by,

$$x_\sigma = \omega_\sigma Z_\sigma(V,T)/Z(V,T) = \omega_\sigma \exp\left(-\frac{F_\sigma(V,T) - F(V,T)}{kT}\right). \tag{10}$$

$S_{conf}(V,T)$ is the entropy due to the mixing of multiple configurations [39]. We approximate it as the uncorrelated probability (avoiding the need for correlated Monte-Carlo calculations):

$$S_{conf}(V,T) = -k_B \sum_\sigma \omega_\sigma \left[\left(\frac{x_\sigma}{\omega_\sigma}\right)\ln\left(\frac{x_\sigma}{\omega_\sigma}\right)\right] = -k_B \sum_\sigma [x_\sigma \ln x_\sigma - x_\sigma \ln \omega_\sigma]. \tag{11}$$

Due to the positive value of entropy, the superposition phase (such as the PM phase) composed of a superposition of periodic configurations is thermally stabilized. It is worthwhile to emphasize that this specific entropy is not the alloy-like entropy due to mixing atoms but rather a different entropy due to mixing configurations of various motifs in a non-alloyed system. As will be demonstrated in subsequent sections, $S_{conf}(V,T)$ plays an important role in the high-temperature disordered phase [39]. Note that the recent work reported by Jones and Stevanovic et al. [61] does not contain the mixing term in the superposition method.

3.2. Computing the thermodynamic quantities from DFT superposition

With the Helmholtz energy of each configuration, as obtained from the DFT-based calculations in Eq. (8), the thermal population of each configuration is computed by minimizing the Helmholtz energy of the superposition phase from Eq. (9), under a given temperature and pressure. Consequently, relevant thermodynamic quantities of the superposition phase can be obtained. For instance, the entropy of the superposition phase is expressed as,

$$S(V,T) = S_{conf}(V,T) + \sum_\sigma x_\sigma S_\sigma(V,T) \tag{12}$$

where $S_\sigma = -(\partial F_\sigma/\partial T)_V$ is the entropy of configuration σ. The heat capacity at constant volume $C_V = -T(\partial^2 F/\partial T^2)_V$ is obtained as,

$$C_V(V,T) = C_{m,V}(V,T) + \sum_\sigma x_\sigma C_{\sigma,V}(V,T) \tag{13}$$

where $C_{\sigma,V}$ is the heat capacity of configuration σ, and $C_{m,V}$ is the magnetic contribution to the heat capacity induced by configurational coupling or spin fluctuations. $C_{m,V}$ is given by

$$C_{m,V}(V,T) = \frac{\beta}{T}\left[\sum_\sigma x_\sigma (E_\sigma)^2 - \left(\sum_\sigma x_\sigma E_\sigma\right)^2\right] \tag{14}$$

where $E_\sigma = F_\sigma + TS_\sigma$ is the energy of configuration σ. The heat capacity at constant pressure can be obtained from $C_p = C_V + \lambda^2 B_T T V$ with λ being the volume thermal expansion coefficient, and the isothermal bulk modulus based on $B_T = V(\partial^2 F/\partial V^2)_T$ given by,

$$\begin{aligned} B_T(V,T) &= B_{m,T}(V,T) + \sum_\sigma x_\sigma B_{\sigma,T}(V,T) \\ &= \beta V\left\{\left[\sum_\sigma x_\sigma P_\sigma\right]^2 - \sum_\sigma x_\sigma (P_\sigma)^2\right\} + \sum_\sigma x_\sigma B_{\sigma,T}(V,T) \end{aligned} \tag{15}$$

where $B_{m,T}$ is the magnetic contribution to isothermal bulk modulus, $B_{\sigma,T}$ the isothermal bulk modulus of configuration σ, and $P_\sigma = -dF_\sigma/dV$.

3.3. The AFM-to-PM Néel transition temperature

An AFM-to-PM phase transition can be either first-order or second-order, which are separated by a critical point [62]. For a first-order transition with respect to temperature, both entropy and heat capacity change discontinuously from one phase to another phase; while in a second-order transition, the entropy changes continuously, and the heat capacity changes discontinuously. Since both AFM and PM phases are superpositions of various spin configurations but with different thermal populations, the second-order transition temperature can be alternatively estimated when the thermal population of the spin ground state configuration decreases to half, which may also be corroborated by the zero macroscopic magnetization [63]. As such, the Néel temperature for the AFM-to-PM phase transition can be estimated from the cross point of the thermal populations between the spin ground state AFM configuration and the summed thermal populations of other spin non-ground state configurations.

4. DFT calculations for total energies of periodic spin configurations

4.1. Details of the DFT calculations

The thermodynamic quantities defined in Sec. III are obtained from the DFT-based calculations. We performed the DFT total energy and force minimization calculations for the periodic spin configurations indicated above in a plane wave basis set with exchange-correlation of the generalized gradient approximation (GGA) with Perdew-Burke-Ernzerhof revised for densely-packed solids and their surfaces (PBEsol) [25,64], as implemented in the Vienna Ab-initio Simulation Package (VASP) [65]. Van der Waals contribution to the energy of 3d perovskites is not considered. The interaction between the ions and valence electrons was described by the projected augmented wave (PAW) method [66,67]. The pseudopotentials were treated with eleven valence electrons for Y ($4s^2 4p^6 4d^1 5s^2$), ten for Ni ($3d^8 4s^2$), and six for O ($2s^2 2p^4$). We employed the DFT + U approach where U_{eff} = U- J with Hubbard U due to the energy increase from an electron addition to a specific site and J due to the screened exchange energy, as introduced by Dudarev et al. [68] for partial removal of unphysical self-interaction. Our evaluation of different U_{eff} values within the range of 0.5–2.0 eV indicated that the U_{eff} = 1.0 eV for the 3d orbital of Ni gives the most consistent description of various magnetic energetics over the range of atomic volumes of

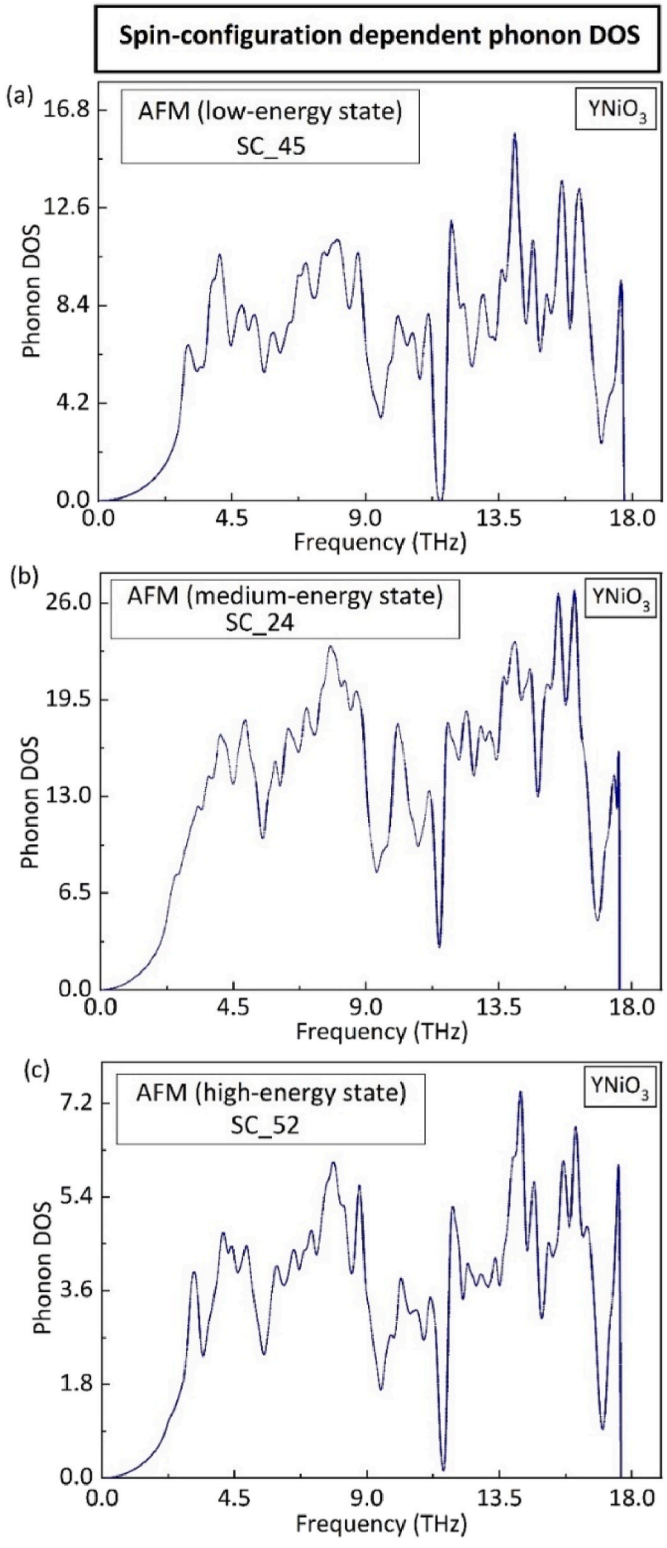

Fig. 3. DFT-calculated configuration-dependent phonon DOS of three spin configurations (SC) in the crystallographic α monoclinic $P2_1/n$ $YNiO_3$ phase, including (a) the spin ground state AFM configuration (SC_45 with the low energy), and (b)–(c) the two AFM configurations above the spin ground state (SC_24 and SC_52 with the medium energy and high energy, respectively).

monoclinic $P2_1/n$ $YNiO_3$. As confirmed in our previous work [57], the predicted local spin moment of the magnetic Ni sites, the highest phonon frequency at the Γ point and the band gap are all in excellent agreement with those values measured from experiments. As such, we used U_{eff} = 1.0 eV for subsequent calculations in the present work. Recall that the U in DFT is not the U in the Hubbard Hamiltonian, as the former acts merely to partially cancel self-interaction but does not represent a strong on-site correlation. Indeed, the numerical value of $U_{eff} = 1.0$ eV in DFT is very different (by a factor of 5 or 10) from the value appropriate for Ni in Hubbard Hamiltonian modeling.

For the first-principles calculations, a plane wave cutoff energy of 520 eV was used. The *k*-point meshes [66] in reciprocal space were the Γ-centered 6×4×4 for the 80-atom supercell. The total energy convergence tolerance was set as 10^{-6} eV/atom. Local spin moment was obtained by integrating the spin density within the PAW spheres (i.e., the setting of LORBIT = 11 in VASP) [69]. For each spin configuration, the 0 K total energy was calculated at seven volumes in the vicinity of equilibrium volume. The resultant energy vs. volume data points were fitted by the four-parameter Birch-Murnaghan equation of state (EOS), based on which the equilibrium volume (V_0), energy (E_0), bulk modulus (B_0), and its pressure derivative (B'_0) can be determined, as shown in Table AIII of Appendix I. The obtained energy for each spin configuration was used as the 0 K energy. i.e., $E_\sigma(V, T = 0)$ in Eq. (8).

4.2. DFT phonon calculations and vibrational contribution to free energy

To obtain the vibrational contribution for the monoclinic $P2_1/n$ $YNiO_3$ phase shown in Fig. 1(b), phonon calculations were performed at five volumes near the equilibrium volume for each of the spin configurations of the α monoclinic $P2_1/n$ $YNiO_3$. Using the supercell approach [70] with VASP as the computational engine, the Hessian matrix and force constants were obtained using the 80-atom 1×2×2 supercell. Fourier transformation of the resultant force constants yields the dynamical matrix, and the diagonalization of the dynamical matrix gives the phonon frequencies and eigenvalues for each selected q point in the reciprocal space. Integration over a large sample of q vectors in the entire Brillouin zone yields phonon density of states (DOS), based on which relevant thermodynamic properties, such as the vibrational free energy and entropy, can be acquired [71]. Fig. 3 shows the calculated phonon DOS at the equilibrium volume of three spin configurations in the α monoclinic $P2_1/n$ insulating $YNiO_3$, including the spin ground state AFM configuration (SC_45) and two other AFM configurations (SC_24 and SC_52) above the spin ground state. There are no imaginary phonon modes, indicating that these spin configurations are dynamically stable at 0 K.

Based on the results of DFT phonon calculations, the vibrational contribution to free energy at finite temperature can be obtained by:

$$F_{vib}(V,T) = k_B T \int_0^\infty \ln\left\{2\sinh\left[\frac{\hbar w}{2k_B T}\right]\right\} g(w)dw \tag{16}$$

where k_B is the Boltzmann constant, $\hbar$ is the Planck constant, w is the phonon frequency, and $g(w)$ is the phonon DOS. The vibrational free energy of Eq. (16) can be used to obtain the single configuration $F_{\sigma,vib}(V,T)$ in Eq. (8). We find that the direct DFT phonon vibrational free energy calculations can be simplified with little loss of accuracy by replacing the more computationally demanding phonon calculations by the Debye model [72], where the Debye temperature is determined from the Debye-Grüneisen model with a nearly constant scale factor s_0, as explained in Appendix II.

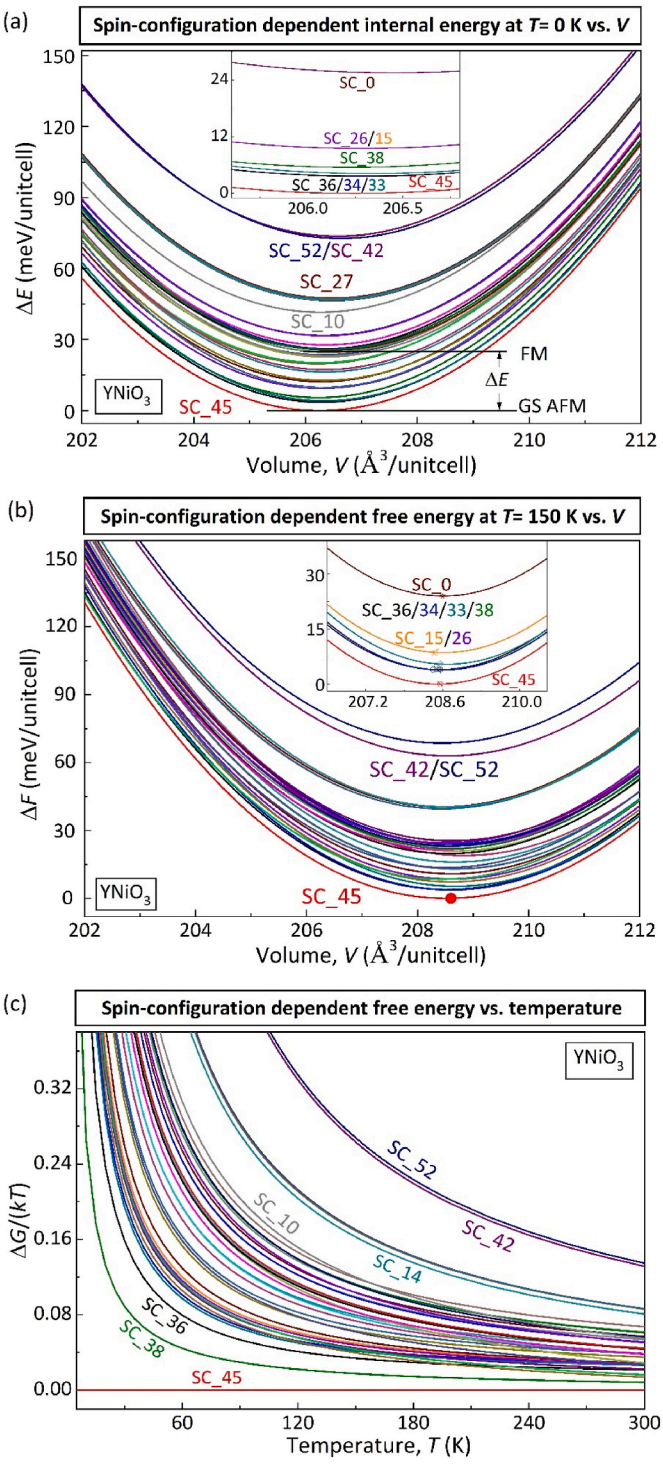

Fig. 4. (a) Relative calculated configuration dependent internal energy ΔE per 20-atom unitcell vs. volume based on Eq. (8) for the 37 independent spin configurations (SC) belonging to the 80-atom 1×2×2 supercell of the α monoclinic $P2_1/n$ $YNiO_3$ at 0 K, and (b) relative Helmholtz energy ΔF at 150 K, together with (c) the relative Gibbs energy ΔG ($G = F + PV$ with P being the pressure) normalized to thermal energy kT for each spin configuration as a function of temperature. The energy vs. volume curves are fitted by the Birch-Murnaghan four-parameter EOS, where the energy of the spin ground state AFM configuration at its theoretical equilibrium volume is taken as the reference state, and the red point indicates the equilibrium volume of the spin ground state AFM configuration. (For interpretation of the references to colour in this figure legend, the reader is referred to the Web version of this article.)

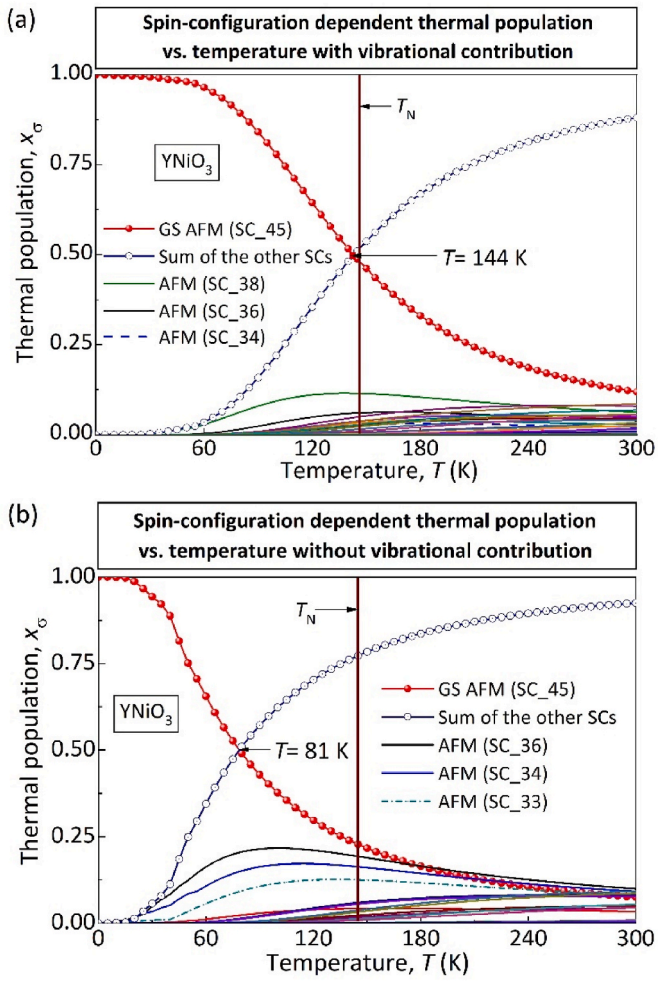

Fig. 5. Temperature-dependent thermal populations for different spin configurations (SC) of the monoclinic $P2_1/n$ $YNiO_3$ at 0 GPa, including the AFM ground state (GS) and the sum over the remained spin configurations (i.e., the spin non-ground state configurations) with (a), and without (b) the vibrational contribution. The solid vertical line denotes the measured Néel temperature (T_N = 145 K) of the monoclinic $P2_1/n$ $YNiO_3$ [44].

5. Results and discussion

5.1. Configurational dependence of volume-minimized internal energy and free energy

The T = 0 K internal DFT energies were obtained for each spin and space configuration belonging to the crystallographic ground state of monoclinic $P2_1/n$ $YNiO_3$. The corresponding internal energy vs. volume plots fitted by the Birch-Murnaghan EOS are shown in Fig. 4(a) for all 37 independent spin configurations, where the reference state is taken as the minimum energy of the spin ground state AFM configuration shown in Fig. 2(f) at its equilibrium volume. The equilibrium volume, energy, bulk modulus, and derivative of bulk modulus with respect to pressure for these individual spin configurations were summarized in Table AIII of Appendix I. There are a number of spin configurations with their energies close to that of the spin ground state AFM configuration. The energy difference between the spin FM configuration and the spin ground state AFM configuration is 25.53 meV per 20-atom unit cell, and was used together with their energy values listed in Table AIII of Appendix I as the 0 K energy in Eq. (8) to calculate the Helmholtz energies for each spin and space configuration.

The Helmholtz energies of these spin configurations at finite temperature were obtained from Eq. (8). Helmholtz energy vs. volume at T = 150 K (i.e., around the Néel temperature) is plotted in Fig. 4(b) with the Helmholtz energy of the spin ground state AFM configuration at its theoretical equilibrium volume, denoted by the red circle, as the reference. The Gibbs energy ($G = F + PV$ with P being the pressure) normalized to thermal energy kT, i.e., $\Delta G/kT$, is presented in Fig. 4(c) with respect to the spin ground state AFM configuration as a function of temperature for the 37 spin configurations of the monoclinic $P2_1/n$ $YNiO_3$ at 0 GPa. The dramatical decrease of $\Delta G/kT$ with respect to the increase of temperature indicates the increase of thermal populations of spin non-ground state configurations at elevated temperatures, as reflected by Eq. (10).

From Fig. 4(a) and (b), one can see that the SC_36 has the lowest internal energy among all spin non-ground state configurations at 0 K, followed by the SC_34, SC_33, SC_38, SC_26, and SC_15 (see also Table AIII in Appendix I, together with their phonon DOS in Figure A1 of Appendix I). However, at 150 K, the SC_38 has the lowest free energy among all spin non-ground state configurations due to the higher entropy of SC_38. SC_38 is followed by the SC_36, SC_34, SC_33, and SC_15 in increasing order of free energy. This is also shown in Fig. 4(c) that the free energy of SC_38 is the closest to that of the SC_45 spin ground state configuration over the temperature range considered.

Fig. 4(a) further shows that the energy curve of the SC_45 spin ground state AFM configuration does not cross any energy curves of spin non-ground state configurations in the volume range plotted. To further study the stability of various spin configurations at 0 K, the energy-volume curves are plotted in Figure A2 of Appendix I with a wider range of volume for the SC_45 spin ground state AFM configuration and the low energy spin non-ground state configurations. It can be seen that the energy curve of the SC_45 spin ground state AFM configuration mergers into the SC_36 at a smaller volume, corresponding to a positive pressure around 17.5 GPa, and at a larger volume, corresponding to a negative pressure around −13.5 GPa (see inserts in Figure A2b). These observations indicate that the transitions between the spin ground state and non-ground state configurations at 0 K are second-order in nature.

5.2. The AFM-to-PM Néel transition and the role of phonons

5.2.1. Configuration-dependent thermal population and Néel transition temperature

Based on Eqs. 9–11, we obtain the temperature evolution of the thermal population coefficients for each spin and space configuration in the superposition phase of monoclinic $P2_1/n$ $YNiO_3$. Fig. 5(a) and (b) show the predicted T-dependent thermal populations of all spin configurations at 0 GPa with and without the vibrational contribution, respectively. As reflected in Fig. 5(a) that below ~50 K the system is dominated by the spin ground state AFM configuration with its thermal population close to 1; above ~50 K, the thermal populations of those spin non-ground state configurations become substantial, and their summation equals to that of the spin ground state AFM configuration at T = 144 K. Because the behavior of the superposition phase reflects the spin-disordering state, the cross point in Fig. 5 with the thermal population of the spin ground state AFM configuration being 0.5 can be defined as the Néel transition temperature (T_N) of monoclinic $P2_1/n$ $YNiO_3$. More spin non-ground state configurations appear above 144 K, with the sum of their thermal populations larger than that of the spin ground state AFM configuration. This indicates the predominance of the spin-disordered PM phase in the monoclinic $P2_1/n$ $YNiO_3$ system. It is remarkable that without fitting parameters the calculated AFM-to-PM transition temperature of 144 K is in good agreement with the experimental observation that the monoclinic $P2_1/n$ $YNiO_3$ system transforms from the spin-ordered AFM phase to the spin-disordered PM phase at ~145 K [44,60,73].

As shown in Fig. 4(c), the spin ground state AFM configuration has the lowest free energy in the temperature range considered under 0 GPa pressure, implying that no transition would take place if we compare the free energy of individual spin configurations, since the spin ground state

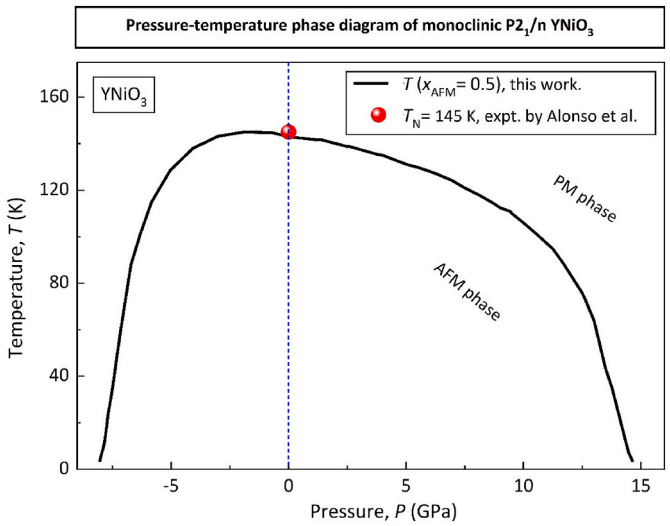

Fig. 6. Calculated AFM-to-PM temperature and pressure (T–P) phase diagram of the monoclinic P2$_1$/n $YNiO_3$ system. The parabolic shape suggests both a positive pressure transition and a negative pressure transition. The black line shows the present prediction from the cross point of thermal populations between the spin ground state AFM configuration and the summation of other spin configurations (i.e., $x_{AFM} = 0.5$). The red sphere denotes the value measured from experiments [44]. (For interpretation of the references to colour in this figure legend, the reader is referred to the Web version of this article.)

AFM configuration should be stable at this temperature range. At the same time, it shows that the free energy difference normalized to the thermal energy decreases dramatically with the increase of temperature, indicating that the thermal populations of those spin non-ground state configurations increase with temperature, as described by Eq. (10). This results in the contribution of magnetic configurational entropy $S_{conf}(V, T)$ to the free energy of the monoclinic P2$_1$/n $YNiO_3$ system, as reflected in Eq. (9). As such, the thermal populations for these spin configurations in monoclinic P2$_1$/n $YNiO_3$ system increase with temperature due to the contribution from $S_{conf}(V, T)$, which makes the prediction of AFM-to-PM phase transition of monoclinic P2$_1$/n $YNiO_3$ system possible.

In typical statistical mechanics, the internal energy is used in the partition function rather than the free energy as in our superposition method, as shown by Eq. (6) [39]. For comparison, Fig. 5(b) plots the thermal populations of all spin configurations without the vibrational contribution in Eq. (8), showing that the thermal population of the SC_45 spin ground state AFM configuration reduces to about half at 81 K, much lower than 144 K with the vibrational entropy included in Fig. 5 (a). This is due to the fact that the vibrational entropies of the majority of spin non-ground state configurations are smaller than that of the spin ground state AFM configuration, as shown in Figure A8 of Appendix II. Consequently, the total thermal population of spin non-ground state configurations without the entropy contribution increases more with temperature than with the vibrational entropy contribution, particularly the SC_36, SC_33, and SC_34 spin non-ground state configurations, as shown in Fig. 5(b). Furthermore, it is observed that the SC_36, SC_34, SC_38 are the dominant spin non-ground state configurations with the vibrational entropy contribution, while the SC_36, SC_33, and SC_34 are the dominant spin non-ground state configurations without the vibrational entropy contribution. This demonstrates the importance of using free energy in the partition function.

5.2.2. *The driving force for AFM-to-PM Néel transition*

To understand the underlying physics associated with the AFM-to-PM phase transition of monoclinic P2$_1$/n $YNiO_3$, we analyzed the connections among free energies of various spin configurations and that of the system, along with the T-dependent thermal population. As shown in Fig. 4, the free energy of all spin non-ground state configurations is higher than that of the spin ground state AFM configuration in the considered temperature range. This indicates that the free energy differences between the spin non-ground state configurations and the spin ground state AFM configuration would not result in variation of spin configurations in the system, as the free energy of the system would increase with the addition of the spin non-ground state configurations. This is reflected by the summation term in Eq. (9). There is also evidence from Eq. (9) that the free energy of the system can be reduced by the last term in Eq. (9), i.e., the magnetic configurational entropy with respect to the competition of the spin ground state and non-ground state configurations. This magnetic configurational entropy increases with temperature, as shown by Fig. 9(b) in Section D, due to the increase of thermal populations of those spin non-ground state configurations, as reflected by Eq. (10) and Fig. 5(a). It is worthwhile to mention that such specific entropy is not the alloy-like entropy due to mixing atoms, but rather a different entropy due to mixing configurations of various motifs in a non-alloyed system.

5.2.3. *The pressure-dependence of the AFM-to-PM Néel transition*

The temperature and pressure phase diagram for the AFM-to-PM phase transition of the monoclinic P2$_1$/n $YNiO_3$ system is depicted in Fig. 6 with the experimental value at 0 GPa denoted by the red sphere. With increasing pressure, the AFM-to-PM transition temperature increases and then decreases. This varying trend of T-P correlation in the monoclinic P2$_1$/n $YNiO_3$ is in correspondence with that reported for other magnetic materials [74]. As shown in both Figs. 5 and 6, an excellent agreement between the present calculation and the experimental measurement is achieved for the AFM-to-PM phase transition in monoclinic P2$_1$/n $YNiO_3$ system at the pressure of 0 GPa.

As the transition temperature approaches 0 K, it is manifested as a phenomenon known as quantum phase transition, which is beyond the scope of the present work. It is noted that the pressure range for the AFM phase at 0 K is between −7.5 and 15 GPa, which is narrower than −13.5 to 17.5 GPa obtained from Figure A2 in Appendix I. This is because the zero-point energy was not included in Figure A2. With increasing temperature, the magnetic configurational entropy becomes more important, which increases the thermal populations of those spin non-ground state configurations and results in the narrower pressure range of the AFM phase region. Fig. 6 shows that the Néel temperature reaches its maximum of 146 K at around −1.15 GPa so that in the negative pressure region, the Néel temperature increases with the increasing pressure; while in the positive pressure region, the Néel temperature decreases with increasing pressure. In comparison with the previous models, the present DFT-based superposition approach can be considered as an improved parameter-free thermodynamic model using the collinear spin configurations. Furthermore, more spin configurations are included in the present superposition approach than in the SQS method for describing the spin-disordered PM phase of $RNiO_3$ [55]. In this context, our temperature-dependent DFT-based thermodynamic model for positionally and magnetically disordered phases provides a predictive approach for investigating the magnetic phase transition of nickelates and the underlying mechanism behind such order-to-disorder phase transition.

5.3. *The polymorphous distribution of magnetic moment*

5.3.1. *Total and local magnetic moment at 0 K*

The distribution of local magnetic moments on Ni sublattice (m_{Ni} for Ni_1–Ni_{16}) in the 37 spin configurations of the monoclinic P2$_1$/n $YNiO_3$ at 0 K is shown in Figure A3(a) of Appendix I, together with their detailed values in Table AII of Appendix I. As discussed above, there are two asymmetrical Ni sites with small and large magnetic moments, which form the centers of the small and large oxygen octahedral clusters in the monoclinic P2$_1$/n $YNiO_3$, respectively. The local magnetic moments of

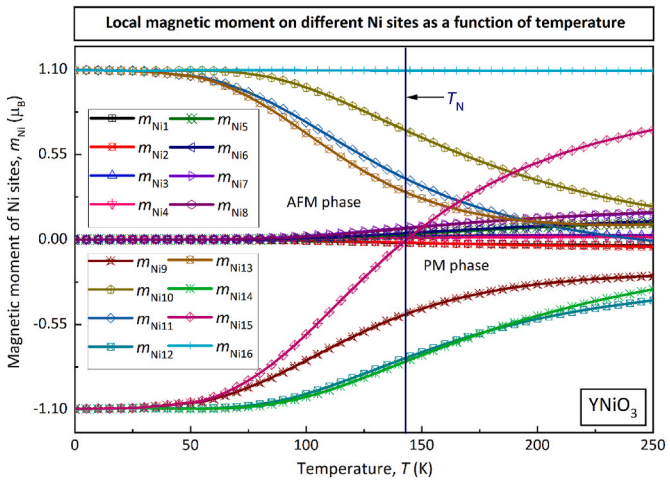

Fig. 7. Predicted Ni-site dependent local magnetic moment as a function of temperature for the monoclinic $P2_1/n$ $YNiO_3$, averaged over the 37 spin configurations based on $m_{Ni} = \sum_{j=0}^{J} x_{\sigma j}(T) \cdot m_{Ni(j)}$, where $x_{\sigma j}(T)$ is the T-dependent thermal population of σ, and $m_{Ni(j)}$ is the corresponding magnetic moment of a specific Ni atom in σ, and $j = 1, 2, \ldots$denotes the 37 spin configurations. The solid vertical line denotes the measured Néel temperature ($T_N = 145$ K) of the monoclinic $P2_1/n$ $YNiO_3$ [44].

Ni sites are within 0.00–0.54 μ_B/atom for Ni_1–Ni_8 and 1.10 μ_B/atom for Ni_9–Ni_{16}. These results are in good agreement with the experimental values measured from magnetic intensities [44], where the two inequivalent Ni sites have the average magnetic moment values of 0.71 and 1.41 μ_B/atom, respectively. The distributions of total magnetic moment (m_{total}) for the 37 spin configurations at $T = 0$ K are present in Figure A3 (b) of Appendix I, arranged into five sets in terms of the total magnetic moment from 0.00 μ_B/80 atom-supercell of AFM configuration to 15.50 μ_B/80 atom-supercell of FM configuration and into subsets in terms of their energies with respect to that of the spin ground state AFM configuration.

5.3.2. *Temperature-dependent local magnetic moment of Ni sites*

Based on the thermal populations and the local magnetic moment on Ni sites in each of these spin configurations, the T-dependent magnetic moment on Ni sites can be evaluated from Eq. (7). Specifically, the average magnetic moment of Ni atom (m_{Ni}) is evaluated by $m_{Ni} = \sum_{j=0}^{J} x_{\sigma j}(T) \cdot m_{Ni(j)}$, where $x_{\sigma j}(T)$ is the T-dependent thermal population of a specific spin configuration σ, and $m_{Ni(j)}$ is the corresponding magnetic moment of a specific Ni atom in σ, and $j = 1, 2, \ldots$denotes the 37 spin configurations in the α monoclinic $P2_1/n$ $YNiO_3$. The variation of the average magnetic moment of each Ni site with respect to temperature is shown in Fig. 7. It can be seen that the average spin moments of the magnetic Ni atoms (i.e., Ni_9–Ni_{16}) decrease from the initial 1.10 μ_B/atom to a value within 0.00–0.50 μ_B/atom as the temperature increases; whereas the average spin moments of those nonmagnetic Ni atoms (i.e., Ni_1–Ni_8) remain around 0.00 μ_B/atom. Below 50 K, the spin ground state AFM configuration with half magnetic Ni atoms (1.10 μ_B/atom) and half nonmagnetic Ni atoms (0.00 μ_B/atom) dominates the system in terms of the average magnetic moment; whereas the average magnetic moment of Ni sites changes gradually above ~50 K, signifying the appearance of the spin-disordering state in the monoclinic $P2_1/n$ $YNiO_3$ system.

To further understand the effect of temperature on magnetic properties, we calculate the temperature-dependent distribution of local moments ($M_{(DL)}$) from the superposition method as: $M_{(DL)} = \sum_j x_{\sigma j}(T) \cdot M_{(DL)_{\sigma j}}$, where $M_{(DL)_{\sigma j}}$ is the spin distribution of σ, and $j = 1, 2, \ldots$corresponds to the 37 spin configurations in the α monoclinic $P2_1/n$ $YNiO_3$. In these calculations, we assumed that there are two equivalent structures (i.e., FM with magnetic moments -μ and FM with magnetic

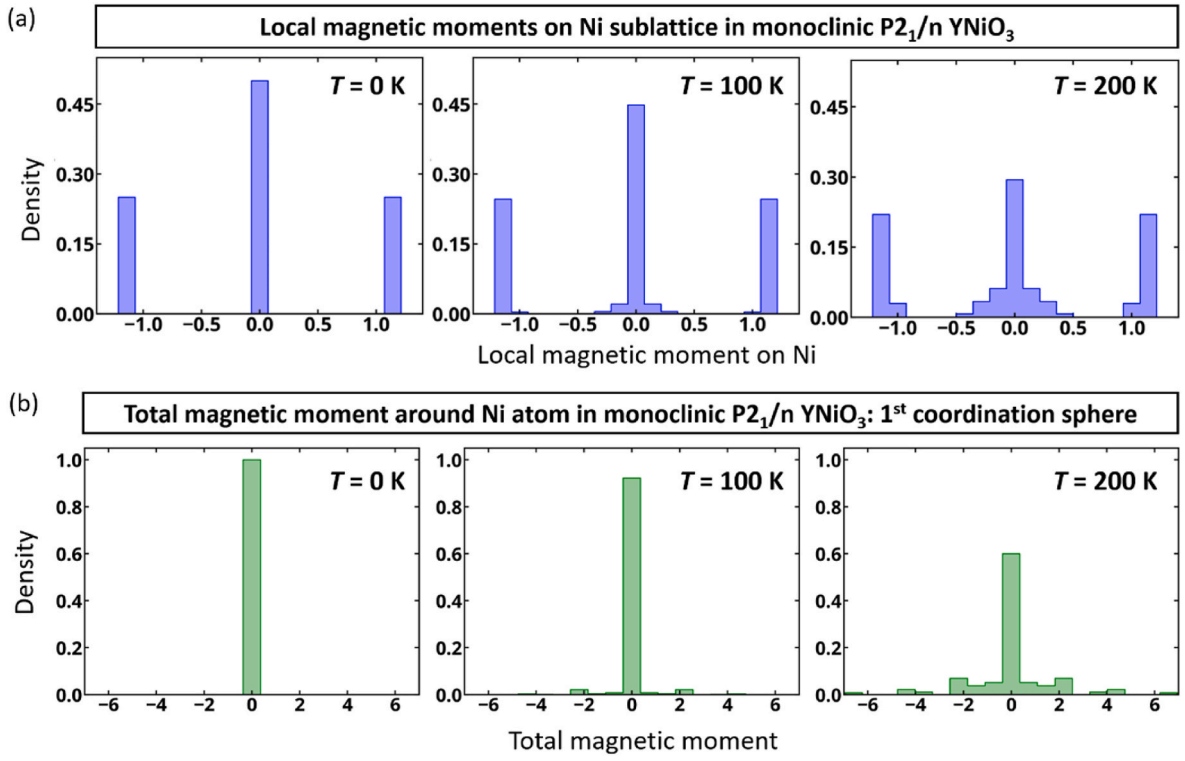

Fig. 8. (a) Temperature-dependence of the distribution of local magnetic moments in the monoclinic $P2_1/n$ $YNiO_3$. (b) Temperature-dependence of the distribution of total magnetic moments around Ni atom in the monoclinic $P2_1/n$ $YNiO_3$ within its 1st coordination sphere. Both effective properties (Pr) are obtained by $Pr = \sum_{j=0}^{J} x_{\sigma j}(T) \times Pr_{\sigma j}$, where $Pr_{\sigma j}$ is the effective property of σ with $j = 1, 2, \ldots$ corresponding to the 37 spin configurations, and $x_{\sigma j}(T)$ is the corresponding thermal population.

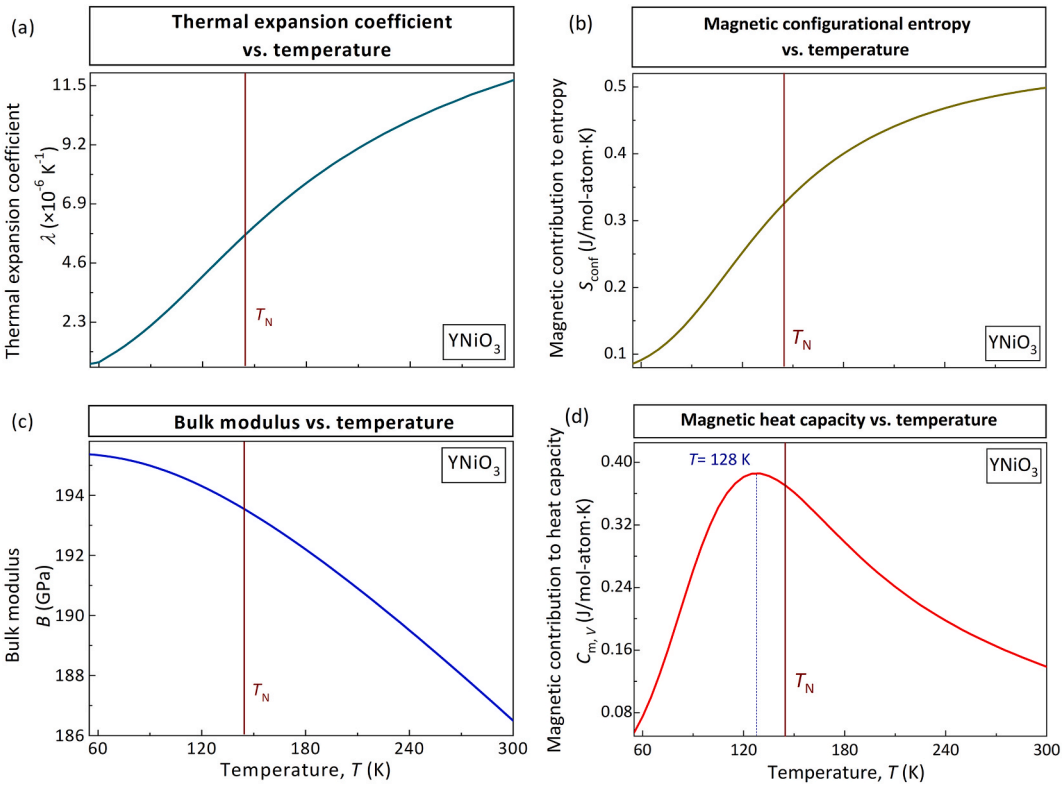

Fig. 9. Predicted thermodynamic quantities of the monoclinic $P2_1/n$ $YNiO_3$ system as a function of temperature from the present superposition approach, including (a) thermal expansion coefficient, (b) magnetic configurational entropy, (c) bulk modulus, and (d) magnetic contribution to heat capacity under the pressure of 0 GPa. The solid vertical line denotes the Néel temperature (T_N = 145 K) of the monoclinic $P2_1/n$ $YNiO_3$ measured in experiment [44].

moment +μ) and that for every spin configuration, there is an equivalent spin configuration where all spins are reversed. The results, shown in Fig. 8(a), demonstrate that while AFM $YNiO_3$ at 0 K can indeed be described as the system having two unique spin environments (i.e., nonmagnetic and magnetic Ni sublattices), the increase of temperature induces broadening of the local spin motifs. Importantly, above 0 K but below T_N, the AFM $YNiO_3$ cannot be described with only two single magnetic moments. For instance, at 100 K, Ni sites in the compressed, small octahedra have magnetic moments in the range of $|0.26| \pm 0.26$ μ_B, while Ni sites in large, expanded octahedra the moments are in the range of $|1.07| \pm 0.09$ μ_B. As the temperature increases above T_N, the distribution of local magnetic moments resembles that found in the spin quasi-random PM models [75]. These results thus demonstrate that paramagnetic phases of Mott insulators cannot be described within nonmagnetic assumption, which has led to the famous (false) breakdown of band theory [76–80], namely predicting zero gap in the PM phase. We now understand that this was not a breakdown of band theory but rather a breakdown of the assumed minimal long-range ordered unit cell [7].

5.4. *Thermodynamic quantities and spin SRO from the DFT superposition approach*

5.4.1. *Temperature-dependent thermodynamic quantities*

The Helmholtz energy of the monoclinic $P2_1/n$ $YNiO_3$ system is obtained from the present superposition approach via Eq. (9). Accordingly, relevant thermodynamic quantities with respect to temperature and volume, including the thermal expansion coefficient, entropy, bulk modulus, and heat capacity of the superposition phase can be derived from Eqs. 12–15. The results are presented in Fig. 9. All these quantities change monotonically with respect to temperature, except the magnetic contribution to heat capacity (i.e., $C_{m,V}$), which exhibits a maximum around 128 K as depicted in Fig. 9(d), indicating a Schottky anomaly. As heat capacity is related to the derivative of entropy to temperature, this suggests the maximum entropy increases around 128 K, which is indeed shown in Fig. 9(b), with the slope reaching the maximum at this temperature. This is reflected in Fig. 5(a) that the thermal populations of the two dominant spin non-ground state configurations, i.e., SC_38 and SC_36, reach their maximum values at around 128 K though the total population of spin non-ground state configurations continues to increase with temperature, but at a descending rate. This is primarily related to magnetic configurational entropy induced by the mixing of various spin configurations, as confirmed in many magnetic materials [63,81,82]. As a second-order transition, such as the present AFM-to-PM transition of monoclinic $P2_1/n$ $YNiO_3$, is defined by the discontinuity in heat capacity of the system, thus this can be correlated to the temperature of maximum heat capacity with the Néel temperature, which is supported by the fact that this temperature is indeed close to the values predicted from both the thermal populations discussed in section B and experimental measurement from magnetic intensity [44,73]. In this context, the magnetic configurational entropy due to thermodynamic fluctuations of spin ground state and non-ground state configurations at finite temperature is responsible for the anomaly variation in heat capacity of the monoclinic $P2_1/n$ $YNiO_3$ system. It is noteworthy that here the specific entropy is not the alloy-like entropy due to mixing atoms, but rather a different entropy due to mixing configurations of various motifs in a non-alloyed system.

5.4.2. *Temperature-dependence of the spin short-range order*

Temperature does not only induce the change of absolute magnetic moments on the Ni sublattice, but also affects the spin SRO. We first calculate the distribution of total magnetic moments around each Ni atom in the first coordination sphere (referenced here as a local magnetic motif) using the superposition approach. The results shown in Fig. 8(b) demonstrate that at $T = 0$ K, the total magnetic moments in the first coordination sphere are always zero – the spins are perfectly

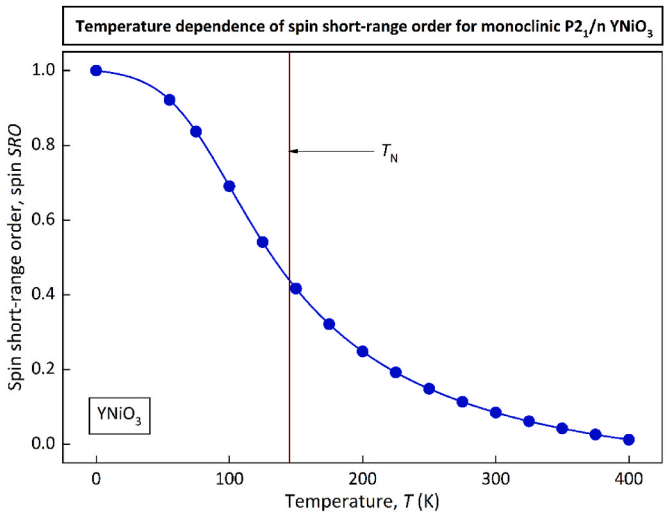

Fig. 10. Temperature-dependence of spin SRO computed as $SRO = 1 - \frac{SD(T)}{SD(SQS)}$, where $SD(T)$ is the standard deviation of the distribution of total magnetic moments around Ni atom in the monoclinic $P2_1/n$ $YNiO_3$ within its 1st coordination sphere, and $SD(SQS)$ is in the spin-SQS model used in Ref. [75]. The solid vertical line denotes the measured Néel temperature ($T_N = 145$ K) of the monoclinic $P2_1/n$ $YNiO_3$ [44].

ordered. Indeed, in the lowest energy AFM monoclinic $P2_1/n$ $YNiO_3$, each magnetic/nonmagnetic Ni site has 6 nonmagnetic/magnetic AFM Ni atoms with accumulated zero magnetic moments. As temperature increases, the zero local spin motifs remain dominant, but there is the appearance of nonzero magnetic motifs, whose contribution increases with temperature, which can be seen by the broadening of distribution of local spin motifs (Fig. 8(b)). All these results can be understood from the breaking spin SRO (Fig. 10), which is calculated as $SRO = 1 - \frac{SD(T)}{SD(SQS)}$, where $SD(T)$ is the standard deviation of the distribution of total magnetic moments around Ni atom in monoclinic $P2_1/n$ $YNiO_3$ within its 1st coordination sphere as computed by the superposition method, and $SD(SQS)$ is in the spin-SQS model (i.e., high-temperature limit of paramagnetic state) used in Ref. [75]. Importantly, these results demonstrate that as temperature increases, the SROs within the first coordination sphere approach that of the spin-SQS model.

6. Conclusions

A superposition approach to density functional thermodynamics on the basis of ensemble partition function with inputs being determined from first-principles calculations is utilized to predict the AFM-to-PM transition of monoclinic disproportionated $P2_1/n$ $YNiO_3$ in the nickelates family. The mixing of various configurations at finite temperature is quantitatively addressed, providing accurate temperature-dependent density functional thermodynamics of positionally and magnetically disordered phase, and revealing the important role of spatial fluctuations in the AFM-to-PM phase transition. It was demonstrated that a complete description of the magnetic transition from the low temperature spin-ordered AFM phase to the high temperature spin-disordered PM phase of monoclinic disproportionated $P2_1/n$ $YNiO_3$ can be achieved. The magnetic configurational entropy, which derives from the competition among spin ground state and non-ground state configurations, is responsible for the occurrence of the AFM-to-PM transition in monoclinic disproportionated $P2_1/n$ $YNiO_3$. The predicted Néel temperature for the monoclinic disproportionated $P2_1/n$ $YNiO_3$ of 144 K at 0 GPa is in good agreement with the experimental value of 145 K. Our investigations offer an improved parameter-free thermodynamic model, and thus provide an alternative method to understand the rich landscape of perovskite nickelates.

Credit author statement

Jinglian Du: Investigation, Calculations, Data curation, Writing, Original draft preparation, Reviewing and Editing, and Validation. Oleksandr Malyi: Data curation, Validation, and Writing, Original draft preparation. Shun-Li Shang: Supervision, Data curation, Methodology, Reviewing and Validation. Yi Wang: Methodology, Reviewing and Validation. Xin-Gang Zhao: Data curation, and Reviewing. Feng Liu: Supervision, and Validation. Alex Zunger: Investigation, Data curation, Supervision, Writing, Original draft preparation, Reviewing and Editing, and Validation. Zi-Kui Liu: Conceptualization, Supervision, Reviewing, , and Editing.

Declaration of competing interest

The authors declare that they have no known competing financial interests or personal relationships that could have appeared to influence the work reported in this paper.

Data availability

Data will be made available on request.

Acknowledgements

JLD is financially supported by the China Scholarship Council, the National Natural Science Foundation of China with Grant No. 52171013, and the Fundamental Research Funds for the Central Universities with Grant No. 3102020QD0412. FL acknowledges the National Natural Science Foundation of China with Grant No. 52130110. JLD, SLS, YW, and ZKL acknowledge the financial support by the Endowed Dorothy Pate Enright Professor at Penn State. First-principles calculations were performed partially on the Roar supercomputer at the Pennsylvania State University's Institute for Computational and Data Sciences (ICDS), partially on the resources of the National Energy Research Scientific Computing Center (NERSC) supported by the U.S. DOE Office of Science User Facility operated under Contract No. DE-AC02-05CH11231, partially on the resources of the Extreme Science and Engineering Discovery Environment (XSEDE) supported by NSF with Grant No. ACI-1548562, and partially on the High-Performance Computing Center of Northwestern Polytechnical University. The authors from CU Boulder (OM, XGZ, and AZ) acknowledge funding from NSF-CMMT DMR with Grant No. 2113922, and the use of Extreme Science and Engineering Discovery Environment (XSEDE) supercomputer resources, which are supported by the National Science Foundation with Grant No. ACI-1548562. The authors are grateful to Dr. Manuel Bibes, Dr. Julien Varignon, Dr. Peilin Liao, and Dr. Pilsun Yoo for valuable suggestions and to Dr. Chelsey Hargather, Dr. W. Chuck Witt, and Patricia Craig for critical reading of the manuscript.

Appendix I. Local magnetic moments of Ni in the 40-atom and 80-atom supercells

This section focuses on the local magnetic moments of Ni sites in different spin configurations at $T = 0$ K, with respect to the reason for setting the initial zero moment of half Ni atoms in the monoclinic $P2_1/n$ $YNiO_3$ phase. The minimum cell of the $YNiO_3$ phase contains ABO_3 formula units (f.u.), i.e., the 20-atom unit cell. Here we firstly use a 40-atom $1 \times \sqrt{2} \times \sqrt{2}$ supercell with eight Ni ions, which appear in a total of 256 spin configurations (SC). These configurations can be further reduced to 63 independent ones by considering the degeneracy factor through the symmetry analysis [56]. We performed DFT total energy calculations for these spin configurations. The results listed in Table AI shows the local magnetic moment of each Ni atom, and total energy with respect to the lowest energy (ΔE) for the 63 independent spin configurations in the 40-atom $1 \times \sqrt{2} \times \sqrt{2}$ supercell of the monoclinic $P2_1/n$ $YNiO_3$. The AFM configuration with minimum energy is taken as the reference state for each case (ΔE). Accordingly, these spin configurations can be grouped in terms of ΔE: including those 15 spin configurations in low energy state (ΔE: 0–6 meV/unitcell), 17 spin configurations in medium energy state (ΔE: 18.8–19.2 meV/unitcell), and the remaining spin configurations in high energy state (ΔE: $>$ 65 meV/unitcell). It is found that the two inequivalent Ni sites in these 63 spin configurations have asymmetrical magnetic moment. Remarkably, those low-energy states are all AFM configurations, where half of the Ni atoms are nonmagnetic with zero spin moment, while the other half are magnetic with spin moment of 1.10–1.19 μ_B/atom. They are labeled as Ni_s and Ni_l being the centers of the small and the large oxygen octahedra in monoclinic $P2_1/n$ $YNiO_3$ phase, respectively, as shown in Table AI. These predicted results are in good correspondence with the experimental measurements [46], where the spin moments of the nonmagnetic Ni site and magnetic Ni site is 0.71 μ_B/atom and 1.41 μ_B/atom, respectively. Since the low-energy configurations are determinative for the present superposition thermodynamic model, the initial magnetic moment of half Ni atoms in the spin configurations of supercells was set as zero for subsequent calculations.

Table AI

Calculated local magnetic moment (m_{Ni}: μ_B/atom) of Ni sites in the 63 independent spin configurations (SC) belonging to the 40-atom $1 \times \sqrt{2} \times \sqrt{2}$ supercell of the monoclinic $P2_1/n$ $YNiO_3$ system, together with the total energy (ΔE: meV per unitcell) relative to the minimum-energy AFM state.

SC_No.	m_{Ni_S}	m_{Ni_S}	m_{Ni_S}	m_{Ni_S}	m_{Ni_L}	m_{Ni_L}	m_{Ni_L}	m_{Ni_L}	ΔE
SC_0	0.56	0.56	0.56	0.56	1.05	1.05	1.05	1.05	18.82
SC_2	0.34	0.16	0.34	0.16	−1.11	1.14	1.04	1.14	19.12
SC_3	0.54	0.54	0.54	0.54	−0.25	−0.25	0.82	0.82	141.15
SC_4	0.00	0.00	0.00	0.00	−1.10	−1.10	1.10	1.10	5.39
SC_5	0.56	0.56	0.56	0.56	1.05	1.05	1.05	1.05	18.82
SC_6	0.13	0.24	0.13	0.24	−1.10	0.16	1.05	0.95	106.32
SC_7	0.16	0.34	0.16	0.34	−1.11	1.14	1.14	1.04	19.09
SC_8	0.00	0.00	0.00	0.00	−1.10	−1.10	1.10	1.10	5.39
SC_9	0.30	0.26	0.26	0.30	−0.32	1.10	−0.32	1.10	172.07
SC_10	0.16	0.34	0.34	0.16	−1.11	1.14	1.04	1.14	19.12
SC_11	0.34	0.16	0.16	0.34	−1.11	1.14	1.14	1.04	19.09
SC_12	0.00	0.00	0.00	0.00	−1.10	−1.10	1.10	1.10	5.39
SC_13	1.19	−1.19	1.19	−1.19	−0.16	0.16	−0.16	0.16	65.91
sC_14	0.13	0.24	0.13	0.24	−1.10	0.16	1.05	0.95	106.21
SC_15	0.28	−0.57	0.26	0.64	−1.07	0.58	0.54	1.00	82.79
SC_16	0.00	0.00	0.00	0.00	−1.10	−1.10	1.10	1.10	5.39
SC_17	−0.86	0.27	−0.86	0.27	0.26	0.26	−0.89	−0.89	153.53
SC_18	0.00	0.00	0.00	0.00	−1.10	−1.10	1.10	1.10	0.00
SC_19	−0.16	−0.34	−0.16	−0.34	−1.14	−1.04	−1.14	1.11	19.09
SC_20	0.17	−0.17	0.17	−0.17	−1.19	−1.19	1.19	1.19	65.08
SC_22	−0.16	−0.34	−0.16	−0.34	−1.14	−1.04	−1.14	1.11	19.09
SC_23	−0.17	0.17	0.17	−0.17	−1.19	−1.19	1.19	1.19	65.08
SC_24	0.00	0.00	0.00	0.00	−1.10	−1.10	1.10	1.10	0.00
SC_25	0.23	0.22	0.22	0.23	0.96	−1.11	−0.15	1.04	97.12
SC_26	0.17	−0.17	0.17	−0.17	−1.19	−1.19	1.19	1.19	65.08
SC_27	0.00	0.00	0.00	0.00	−1.10	−1.10	1.10	1.10	0.00
SC_29	−0.56	−0.56	−0.56	−0.56	−1.05	−1.05	−1.05	−1.05	18.82
SC_30	−0.82	−0.52	−0.82	−0.52	−0.76	−0.85	−0.85	0.24	76.68
SC_31	−0.17	0.17	−0.17	0.17	−1.19	−1.19	1.19	1.19	69.08
SC_32	−0.34	−0.16	−0.34	−0.16	−1.04	−1.14	−1.14	1.11	19.12
SC_33	0.17	−0.17	−0.17	0.17	−1.19	−1.19	1.19	1.19	65.08
SC_34	−0.16	−0.34	−0.34	−0.16	−1.04	−1.14	−1.14	1.11	19.12
SC_35	−0.17	0.17	−0.17	0.17	−1.19	−1.19	1.19	1.19	65.08
SC_37	−0.56	−0.56	−0.56	−0.56	−1.05	−1.05	−1.05	−1.05	18.82
SC_41	−0.91	−0.91	−0.07	−0.07	−1.03	−0.04	−1.03	−0.04	133.35
SC_42	−0.17	−0.17	−0.25	−0.25	−1.04	−0.16	1.11	−0.94	102.28
SC_43	−0.03	−0.03	0.19	0.19	−1.01	1.16	1.16	0.15	140.49
SC_44	0.00	0.00	0.00	0.00	−1.10	−1.10	1.10	1.10	5.39
SC_45	−1.10	−1.10	1.10	1.10	0.00	0.00	0.00	0.00	0.71
SC_46	0.22	0.23	0.23	0.22	−1.11	0.96	1.04	−0.15	97.50
SC_47	0.15	0.24	0.24	0.15	−1.11	0.95	0.17	1.05	102.81
SC_48	0.00	0.00	0.00	0.00	−1.10	−1.10	1.10	1.10	5.39
SC_49	0.17	−0.17	0.17	−0.17	−1.19	1.19	−1.19	1.19	65.08
SC_50	0.34	0.16	0.34	0.16	−1.11	1.14	1.04	1.14	19.12
SC_51	0.16	0.34	0.16	0.34	−1.11	1.14	1.14	1.04	19.09
SC_53	0.17	0.17	−0.17	−0.17	−1.19	−1.19	1.19	1.19	65.08
SC_54	0.00	0.00	0.00	0.00	−1.10	−1.10	1.10	1.10	0.00
SC_56	−0.17	0.17	0.17	−0.17	−1.19	−1.19	1.19	1.19	65.08
SC_57	0.00	0.00	0.00	0.00	−1.10	−1.10	1.10	1.10	0.00
SC_62	−0.17	−0.17	0.17	0.17	−1.19	−1.19	1.19	1.19	65.08

(continued on next page)

Table AI (*continued*)

SC_No.	m_{Ni_S}	m_{Ni_S}	m_{Ni_S}	m_{Ni_S}	m_{Ni_L}	m_{Ni_L}	m_{Ni_L}	m_{Ni_L}	ΔE
SC_64	0.17	−0.17	−0.17	0.17	−1.19	−1.19	1.19	1.19	65.08
SC_71	0.27	0.27	−0.86	−0.86	0.26	−0.89	0.26	−0.89	153.53
SC_72	0.08	0.08	0.24	0.24	−1.06	1.15	−0.26	1.15	136.17
SC_73	−0.15	−0.15	−0.24	−0.24	−1.05	−0.17	−0.95	1.11	102.86
SC_74	0.00	0.00	0.00	0.00	−1.10	−1.10	1.10	1.10	5.39
SC_76	0.34	0.16	0.16	0.34	−1.11	1.14	1.04	1.14	19.12
SC_77	0.16	0.34	0.34	0.16	−1.11	1.14	1.14	1.04	19.09
SC_79	−0.17	−0.17	0.17	0.17	−1.19	−1.19	1.19	1.19	65.08
SC_80	0.00	0.00	0.00	0.00	−1.10	−1.10	1.10	1.10	0.00

Then the 8 f,u. 40-atom supercell was raised to a minimum base cell of 16 f.u. (16 Ni-centered octahedra), i.e., 80 atoms of the $P2_1/n$ $YNiO_3$. There are 35 possible 80-atom supercells in terms of the spatial arrangements of four 20-atom base cells. Populating such an 80-atom supercell by restricting the initial spin configuration (i.e., prior to the self-consistent calculation) to be 8 Ni atoms with zero moments and 8 Ni atoms with nonzero moments, creates 256 spin configurations for each supercell, of which 37 are symmetry independent for the 80-atom 1×2×2 supercell used in the present work. Table AII lists the calculated local magnetic moment of 16 Ni atoms in the 37 independent spin configurations belonging to the 80-atom 1×2×2 supercell of the monoclinic $P2_1/n$ $YNiO_3$. It turns out that these 16 Ni atoms can be classified into two types, i.e., the nonmagnetic Ni sites including Ni_1–Ni_8 with spin moment of 0–0.54 μ_B/atom, and the magnetic Ni sites including Ni_9–Ni_{16} with spin moment of 1.10 μ_B/atom. Their distributions are depicted in Figure A3 and are consistent with both those determined from the 40-atom supercell and those measured from experiments. Table AIII shows the results of energy-volume fitting data for the 37 independent spin configurations of the 80-atom 1×2×2 supercell, and their corresponding multiplicity. The next step beyond the 16 f.u. cell (80-atom cell) is a 32 f.u. cell (160-atom cell) with 155 unique supercells in terms of the spatial arrangements of eight 20-atom base cells. There are 65536 spin configurations obtained by considering half of the Ni atoms for each supercell as nonmagnetic, and only 4992 are independent configurations for the 160-atom 2×2×2 supercell. Table AIV provides relevant number of supercells and spin configurations of the monoclinic $P2_1/n$ $YNiO_3$ involved in the finite temperature superposition method. The present work focuses on the 80-atom 1×2×2 supercell as the base model for the *monoclinic* $P2_1/n$ $YNiO_3$ system.

Table AII
Calculated local spin moment (m_{Ni}: μ_B) of Ni atoms in the 37 independent spin configurations (SC) belonging to the 80-atom 1×2×2 supercell of monoclinic $P2_1/n$ $YNiO_3$ system.

SC_No.	m_{Ni1}	m_{Ni2}	m_{Ni3}	m_{Ni4}	m_{Ni5}	m_{Ni6}	m_{Ni7}	m_{Ni8}	m_{Ni9}	m_{Ni10}	m_{Ni11}	m_{Ni12}	m_{Ni13}	m_{Ni14}	m_{Ni15}	m_{Ni16}
SC_0	0.54	0.54	0.54	0.54	0.54	0.54	0.54	0.54	1.06	1.06	1.06	1.06	1.06	1.06	1.06	1.06
SC_2	0.36	0.17	0.51	0.17	0.36	0.49	0.50	0.49	−1.10	1.11	1.03	1.11	1.08	1.11	1.08	1.11
SC_3	0.17	0.36	0.17	0.51	0.49	0.36	0.49	0.51	1.10	−1.11	1.11	1.03	1.11	1.08	1.11	1.08
SC_4	0.01	0.01	0.18	0.18	0.33	0.33	0.49	0.49	−1.10	−1.10	1.07	1.07	1.11	1.11	1.11	1.11
SC_5	0.33	−0.17	0.33	−0.17	0.33	0.48	0.33	0.48	−1.15	1.14	−1.15	1.14	1.08	1.14	1.08	1.14
SC_6	0.18	0.01	0.01	0.18	0.49	0.33	0.33	0.49	1.07	−1.10	−1.10	1.07	1.11	1.10	1.10	1.11
SC_7	0.01	−0.31	0.01	−0.17	0.32	0.33	0.32	0.47	1.14	−1.08	−1.14	1.09	1.11	1.13	1.11	1.14
SC_8	−0.16	0.33	−0.16	0.33	0.48	0.33	0.48	0.33	1.15	−1.15	1.15	−1.15	1.15	1.09	1.15	1.09
SC_9	−0.31	0.01	−0.17	0.01	0.33	0.32	0.47	0.32	−1.08	−1.14	1.09	−1.14	1.13	1.11	1.14	1.11
SC_10	−0.31	−0.31	−0.31	−0.31	0.31	0.31	0.31	0.31	−1.13	−1.13	−1.13	−1.13	1.13	1.13	1.13	1.13
SC_11	0.19	0.17	0.49	0.17	0.19	0.17	0.49	0.17	−1.13	1.14	1.05	1.14	−1.13	1.14	1.05	1.14
SC_12	−0.16	0.00	0.17	0.18	0.18	0.00	0.49	0.18	−1.12	−1.08	1.07	1.09	−1.12	1.12	1.08	1.12
SC_13	0.34	0.16	0.34	0.16	0.34	0.16	0.34	0.16	1.04	1.14	−1.10	1.14	−1.10	1.14	1.04	1.14
SC_14	0.17	−0.16	0.32	−0.16	0.17	0.16	0.32	0.16	−1.18	1.17	−1.15	1.17	−1.13	1.17	1.04	1.17
SC_15	0.01	0.01	0.01	0.17	0.33	0.01	0.33	0.17	1.07	−1.09	−1.10	1.10	−1.10	1.12	1.07	1.13
SC_16	−0.16	−0.31	0.00	−0.17	0.170.00	0.00	0.31	0.16	−1.16	−1.07	−1.14	1.11	−1.11	1.14	1.07	1.16
SC_17	−0.48	0.00	−0.18	0.00	0.18	0.00	0.48	0.00	−1.10	−0.98	1.10	−0.98	−1.10	0.98	1.10	0.98
SC_18	0.01	0.17	0.01	0.01	0.33	0.17	0.33	0.01	1.07	1.10	−1.10	−1.09	−1.10	1.13	1.07	1.12
SC_19	−0.16	−0.17	0.00	−0.32	0.17	0.16	0.32	0.00	−1.15	1.11	−1.14	−1.06	−1.11	1.15	1.06	1.14
SC_20	−0.33	0.00	−0.33	0.00	0.33	0.00	0.33	0.00	1.08	−0.98	−1.08	−0.98	−1.08	0.98	1.08	0.98
SC_22	0.17	0.19	0.17	0.49	0.17	0.19	0.17	0.49	1.14	−1.13	1.14	1.05	1.14	−1.13	1.14	1.05
SC_23	0.00	−0.16	0.18	0.17	0.00	0.18	0.18	0.48	−1.08	−1.12	1.09	1.07	1.12	−1.12	1.12	1.08
SC_24	0.00	−0.48	0.00	−0.18	0.00	0.18	0.00	0.48	−0.98	−1.10	−0.98	1.10	0.98	−1.10	0.98	1.10
SC_25	0.16	0.34	0.16	0.34	0.16	0.34	0.16	0.34	1.14	1.04	1.14	−1.11	1.14	−1.11	1.14	1.04
SC_26	0.01	0.01	0.16	0.01	0.01	0.33	0.16	0.33	−1.09	1.07	1.10	−1.10	1.12	−1.10	1.13	1.07
SC_27	−0.16	0.17	−0.16	0.32	0.17	0.17	0.16	0.32	1.17	−1.18	1.17	−1.15	1.17	−1.13	1.17	1.04
SC_28	−0.31	−0.16	−0.17	0.00	0.00	0.17	0.16	0.32	−1.06	−1.15	1.11	−1.14	1.14	−1.11	1.15	1.06
SC_29	0.17	0.01	0.01	0.01	0.17	0.33	0.01	0.33	1.10	1.07	−1.09	−1.10	1.13	−1.10	1.12	1.07
SC_30	0.00	−0.33	0.00	−0.33	0.00	0.33	0.00	0.33	−0.98	1.08	−0.98	−1.08	0.98	−1.08	0.98	1.08
SC_31	−0.17	−0.16	−0.32	0.00	0.16	0.17	0.00	0.32	1.11	−1.16	−1.06	−1.14	1.16	−1.11	1.14	1.06
SC_33	−0.18	−0.18	0.18	0.18	−0.18	−0.18	0.18	0.18	−1.10	−1.10	1.10	1.10	−1.10	−1.10	1.10	1.10
SC_34	0.00	−0.16	0.00	0.16	0.00	−0.16	0.00	0.16	1.09	−1.11	−1.09	1.11	−1.09	−1.11	1.09	1.11
SC_36	−0.16	0.00	0.16	0.00	−0.16	0.00	0.16	0.00	−1.11	1.09	1.11	−1.09	−1.11	−1.09	1.11	1.09
SC_38	0.00	0.00	0.00	0.00	0.00	0.00	0.00	0.00	1.10	1.10	−1.10	−1.10	−1.10	−1.10	1.10	1.10
SC_42	0.15	−0.15	0.15	−0.15	0.15	−0.15	0.15	−0.15	−1.16	1.16	−1.16	1.16	−1.16	1.16	−1.16	1.16
SC_45	0.00	0.00	0.00	0.00	0.00	0.00	0.00	0.00	−1.10	1.10	1.10	−1.10	1.10	−1.10	−1.10	1.10
SC_52	−0.16	0.16	−0.16	0.16	−0.16	0.16	−0.16	0.16	1.19	−1.19	1.19	−1.19	1.19	−1.19	1.19	−1.19

Table AIII
Physical quantities of the 37 independent spin configurations (SC) belonging to the 80-atom 1×2×2 supercell of the monoclinic of $P2_1/n$ $YNiO_3$ system, including the equilibrium volume (V_0: $Å^3$ per 20-atom unitcell), bulk modulus (B_0: GPa) and its pressure derivative (B_0'), together with the energy (ΔE_0: meV per 20-atom unitcell) relative to the spin ground state AFM configuration (SC_45), and the corresponding multiplicity for each spin configuration.

SC_No.	V_0	B_0	B'_0	ΔE_0	Multiplicity
SC_0	206.45	196.59	4.21	25.53	2
SC_2	206.41	197.17	4.44	24.68	8
SC_3	206.41	197.22	4.45	24.61	8
SC_4	206.34	198.98	4.84	17.32	16
SC_5	206.46	194.26	3.86	47.14	4
SC_6	206.35	197.71	4.54	16.35	16
SC_7	206.34	195.15	4.23	31.66	16
SC_8	206.46	194.32	3.89	47.04	4
SC_9	206.32	195.05	4.35	31.72	16
SC_10	206.26	193.39	4.51	41.57	4
SC_11	206.41	196.73	4.32	26.08	4
SC_12	206.33	197.97	4.57	12.77	16
SC_13	206.39	196.79	4.09	23.08	4
SC_14	206.45	195.00	4.06	46.64	8
SC_15	206.28	197.52	4.53	9.52	8
SC_16	206.32	195.72	4.36	26.04	8
SC_17	206.31	194.55	4.29	23.54	4
SC_18	206.28	197.42	4.53	12.28	8
SC_19	206.34	195.26	4.15	27.70	8
SC_20	206.24	194.04	4.26	20.16	4
SC_22	206.40	196.18	4.28	25.77	4
SC_23	206.34	197.90	4.56	12.78	16
SC_24	206.31	194.53	4.28	23.56	4
SC_25	206.35	197.15	4.47	22.71	4
SC_26	206.28	197.54	4.53	9.50	8
SC_27	206.46	194.63	3.92	46.97	8
SC_28	206.32	195.70	4.36	26.03	8
SC_29	206.27	197.40	4.53	12.30	8
SC_30	206.21	194.61	4.60	19.76	4
SC_31	206.34	195.23	4.14	27.73	8
SC_33	206.33	198.22	4.58	4.18	4
SC_34	206.28	197.78	4.50	3.63	4
SC_36	206.28	197.80	4.50	3.60	4
SC_38	206.23	197.26	4.48	5.52	2
SC_42	206.57	193.41	3.88	73.61	1
SC_45	206.24	197.56	4.43	0	2
SC_52	206.62	194.68	3.62	72.69	1

Table AIV
Relevant information of the monoclinic $P2_1/n$ $YNiO_3$ involved in the superposition method, including the number of formula unit, the number of atoms, the number of supercells, the objective supercell, the corresponding number of spin configurations and the number of unique spin configurations in each case. Note that the number of spin configurations in the 40-atom $1 \times \sqrt{2} \times \sqrt{2}$ supercell is created by considering initial non-zero magnetic moment of all Ni sites, whereas that in the 80-atom 1×2×2 supercell and the 160-atom 2×2×2 supercell are created by considering initial non-zero magnetic moment of half of the Ni atoms.

Number of formula unit	Number of atoms (atoms/cell)	Numbers of such supercell	Objective supercell	Number of spin configurations	Number of unique spin configurations
4	20	1	1×1×1	1	1
8	40	7	$1 \times \sqrt{2} \times \sqrt{2}$	256	63
16	80	35	1×2×2	256	37
32	160	155	2×2×2	65536	4992

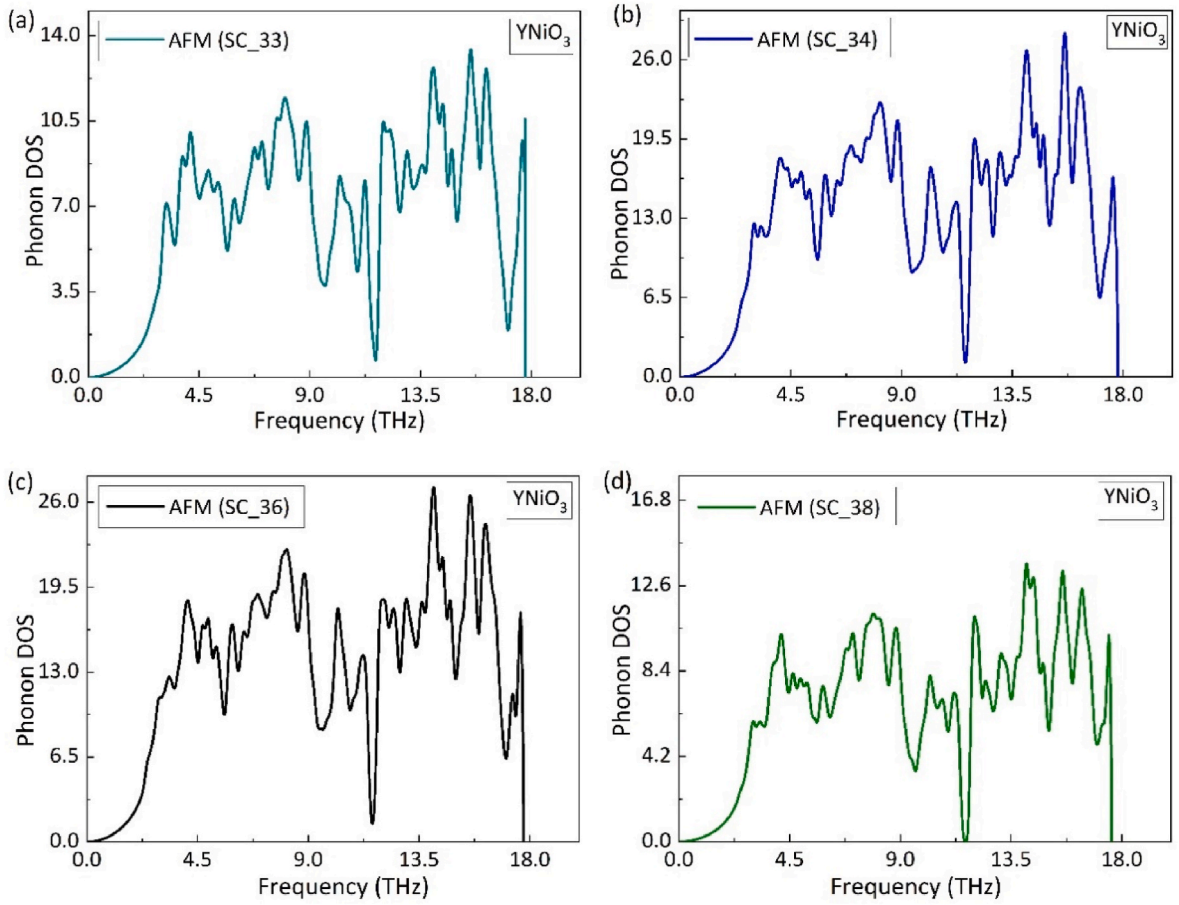

Fig. A1. Calculated configuration-dependent phonon density of state (DOS) of four spin configurations (SC) in the monoclinic $P2_1/n$ $YNiO_3$, i.e., SC_33 (a), SC_34 (b), SC_36 (c), and SC_38 (d), respectively.

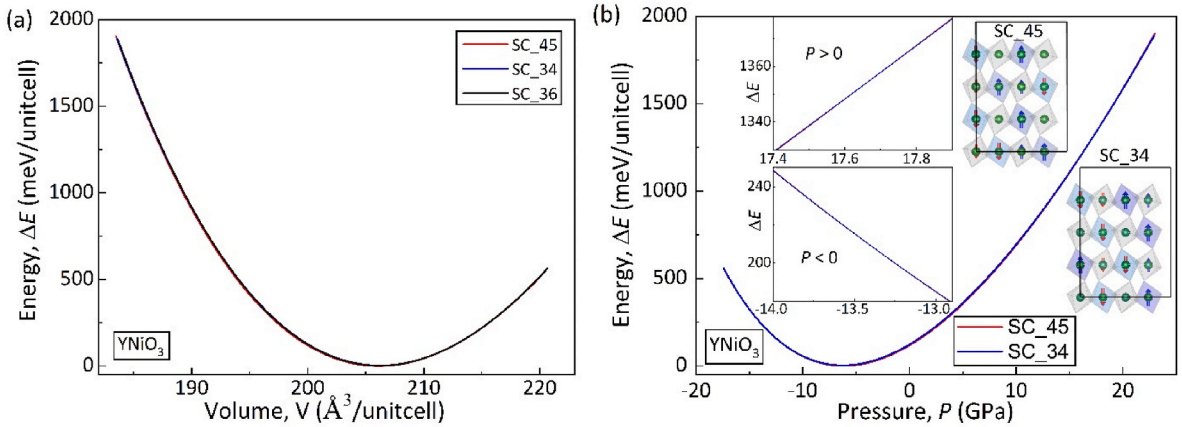

Fig. A2. Calculated configuration-dependent energy-volume (a), and energy-pressure (b) diagrams at 0 K for the spin ground state configuration SC_45 and non-ground state configuration SC_34, with the spin configurations and the second-order transition pressure shown as inserts in (b).

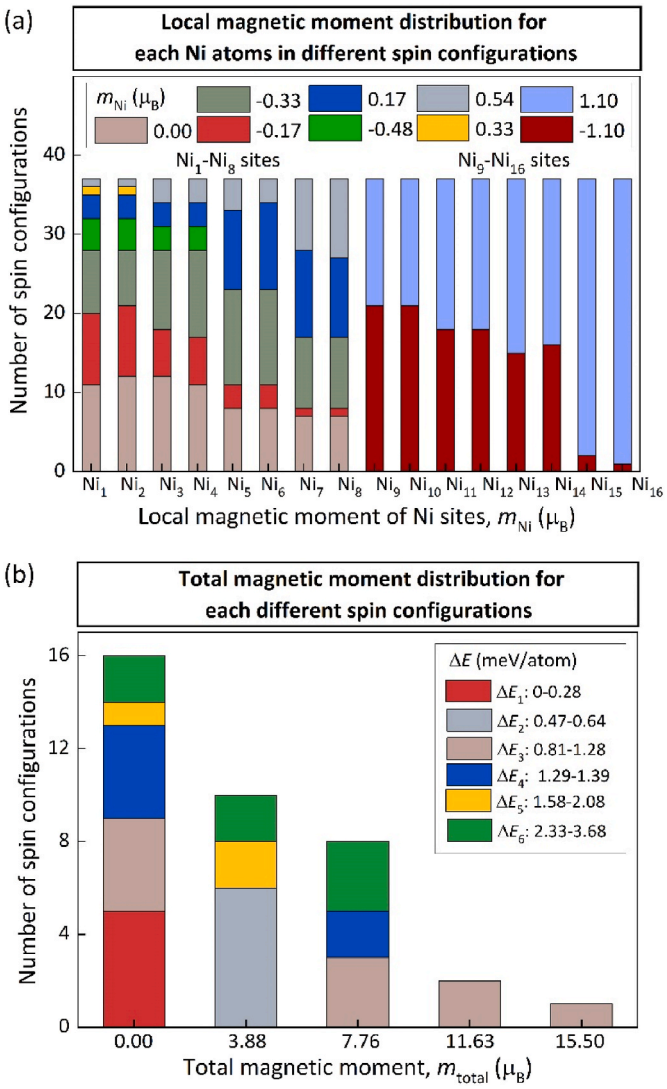

Fig. A3. Ni-site dependent magnetic moment of the monoclinic $P2_1/n$ $YNiO_3$. (a) Distribution of the local magnetic moments on 16 Ni atoms (m_{Ni}) in the 37 independent spin configurations belonging to the 80-atom 1×2×2 supercell of monoclinic $P2_1/n$ $YNiO_3$. Two inequivalent Ni sites are distinguished by the nonmagnetic Ni atoms from Ni_1 to Ni_8 with m_{Ni} = 0.00–0.54 μ_B/atom, and the Ni atoms from Ni_9 to Ni_{16} with m_{Ni} denoted by m_{Ni} = 1.10 μ_B/atom. (b) Histograms of the total magnetic moment for each of the 37 independent spin configurations belonging to the 80-atom 1×2×2 supercell of monoclinic $P2_1/n$ $YNiO_3$ at 0 K, based on which these spin configurations are arranged into five groups with their energy relative to the spin ground state AFM configuration provided in the insert.

Appendix II. Vibrational contribution to the free energy: fitting the Debye model to DFT phonon thermodynamics

This section focuses on the lattice vibrational contribution to thermodynamics at finite temperature, and the evidence of how closely the Debye model agrees with the DFT phonon free energy for different excited states.

Debye model approximation to the phonon free energy

As an alternative method to more computationally demanding phonon calculations, the Debye model for estimating the lattice vibrational contribution to free energy is given by:

$$F_{vib}(V,T) = \frac{9}{8}k_B\Theta_D + k_BT\left\{3\ln\left[1-\exp\left(-\frac{\Theta_D}{T}\right)\right] - D\left(\frac{\Theta_D}{T}\right)\right\} \quad \text{(A1)}$$

where Θ_D is the Debye temperature, $D(\Theta_D/T)$ is the Debye function. Θ_D can be determined from the Debye-Grüneisen model via:

$$\Theta_D = s_0 A V_0^{1/6}\left(\frac{B_0}{M}\right)^{1/2}\left(\frac{V_0}{V}\right)^{\gamma} \quad \text{(A2)}$$

where s_0 is the scaling factor, B_0 is the bulk modulus, M is the average atomic mass, $A = (6\pi^2)^{1/3}(\hbar/k_B)$ is a constant of 231.04 if V in Å^3 and B in GPa, γ is the Grüneisen parameter given by $\gamma = [(1+B_0')/2 - x]$ with $x = 2/3$ for high temperature condition and $x = 1$ for low temperature condition. The

usefulness of the Debye model depends on whether the scaling factor s_0 that produces an agreement between the Debye model, and the explicit DFT phonon calculations of free energy will depend strongly or weakly on the spin non-ground state configurations (e.g., SC_24 and SC_52) in the supercell. As shown in Figure A4, we tested this by comparing the Helmholtz energies from the phonon DOS presented in Fig. 3 in the main text. It is found that s_0 is close to each other, i.e., $s_0 = 0.906$ for the high-energy AFM state SC_52, and $s_0 = 0.861$ for the medium-energy AFM state SC_24, and $s_0 = 0.898$ for the low-energy AFM state SC_45.

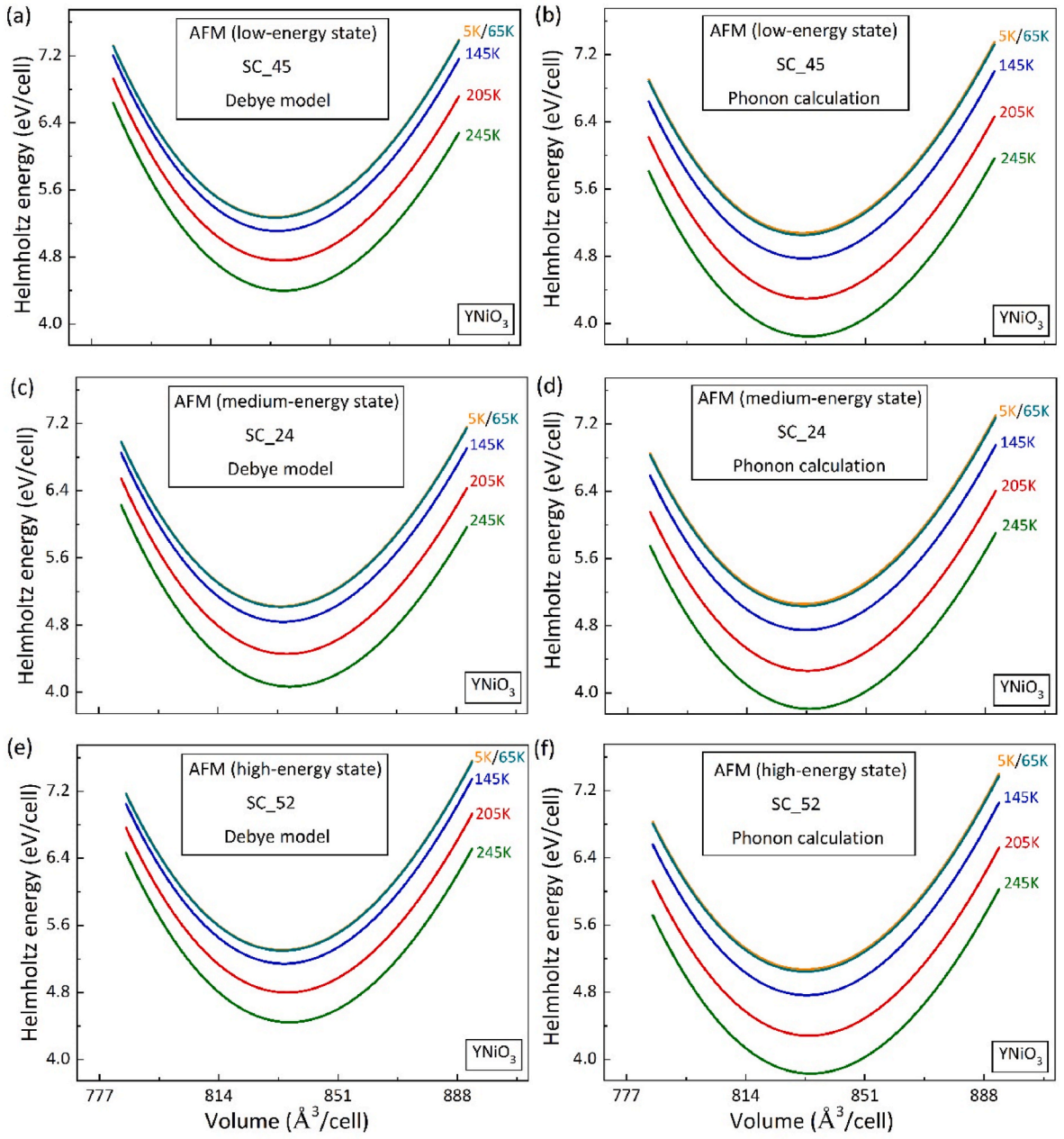

Fig. A4. Calculated configuration-dependent Helmholtz energy (eV/cell-80atoms) as a function of volume (Å^3/cell-80 atoms) predicted by the Debye model and the phonon calculations for the AFM configuration SC_45 at the spin ground state (a, b), as well as two AFM configurations above the spin ground state of SC_24 with medium energy (c, d) and SC_52 with high energy (e, f) of the monoclinic $P2_1/n$ $YNiO_3$ at different temperature conditions.

Evidence of how closely Debye model reproduced DFT phonon free energy

As such, we make a systematic comparison for the vibrational contribution to free energy, and relevant thermodynamic properties of the monoclinic $P2_1/n$ $YNiO_3$. The according thermodynamic quantities (including heat capacity C_p, entropy S, enthalpy H, and Gibbs energy G) of the AFM configurations at the low-energy, medium-energy and high-energy state (i.e., the spin ground state AFM configuration of SC_45, as well as the two spin non-ground states AFM configurations of SC_24 and SC_52), predicted by the DFT phonon calculations in comparison with those by the Debye model under zero external pressure are shown in Figure A5, Figure A6 and Figure A7, respectively. Noting that the results predicted by Debye model with $s_0 = 0.617$, the value of which is usually used for metallic system, are also presented in Figure A5 for comparison. It turns out that the thermodynamic properties predicted by the Debye model are in good correspondence with those by the DFT phonon calculations. This indicates that reasonable results can be obtained from the Debye model without performing the time-consuming first-principles phonon calculations for all of these spin configurations. As such, we demonstrated that the Debye model do not change the main physics of the present work. Accordingly, the Debye model with $s_0 = 0.9$ was used to acquire the vibrational contribution of individual spin configuration in the present work, i.e., $F_{\sigma,vib}(V,T)$ in Eq. (8). The entropy of the 37 independent spin configurations in the monoclinic $P2_1/n$ $YNiO_3$ system as a function of temperature under the pressure of 0 GPa was shown in Figure A8, where the entropy of spin ground state AFM configuration is taking as a reference.

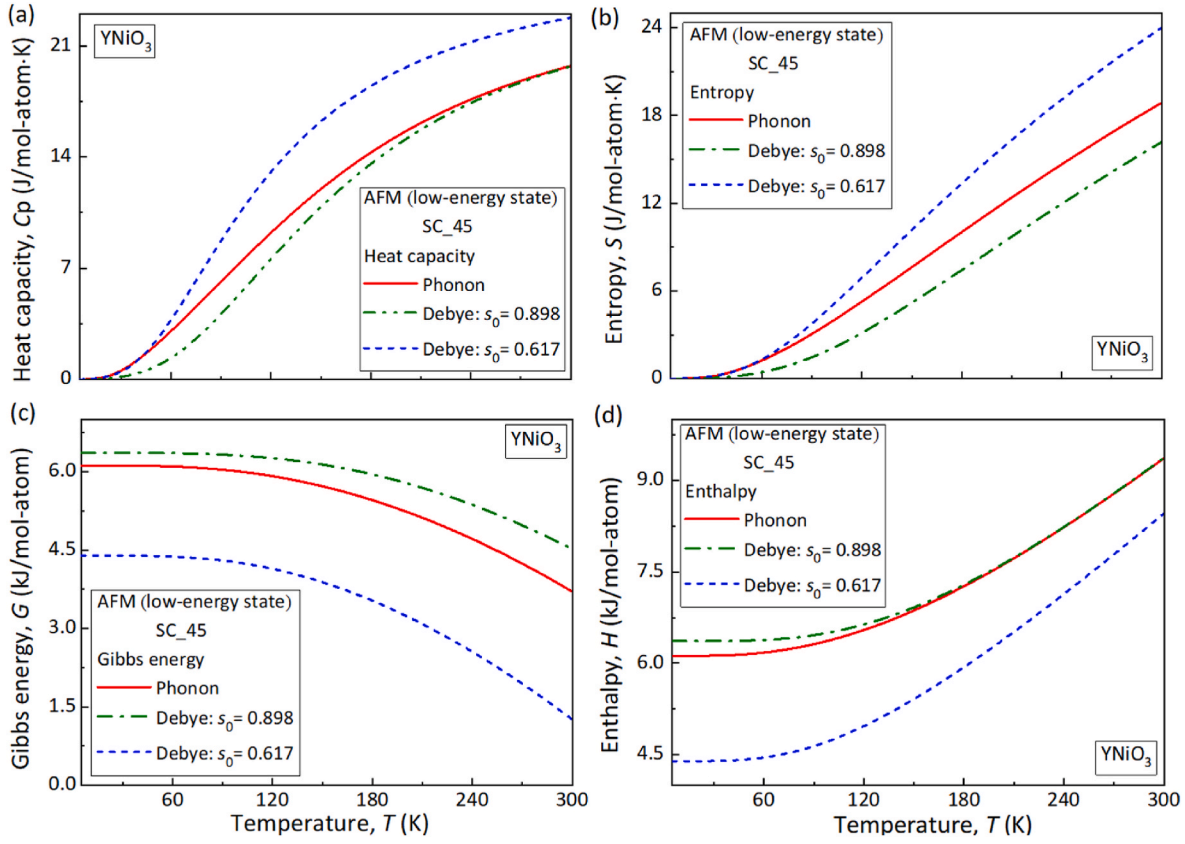

Fig. A5. Calculated configuration-dependent thermodynamic quantities at finite temperature of the spin ground state AFM configuration (SC_45 with low energy) for the monoclinic $P2_1/n$ $YNiO_3$ obtained by the DFT phonon calculations (red solid line) and the Debye model ($s_0 = 0.898$ fitted to phonon data in green dot-dashed line and $s_0 = 0.617$ commonly used for metals in blue dotted line), including (a) Heat capacity Cp, (b) Entropy S, (c) Gibbs energy G, and (d) Enthalpy H.

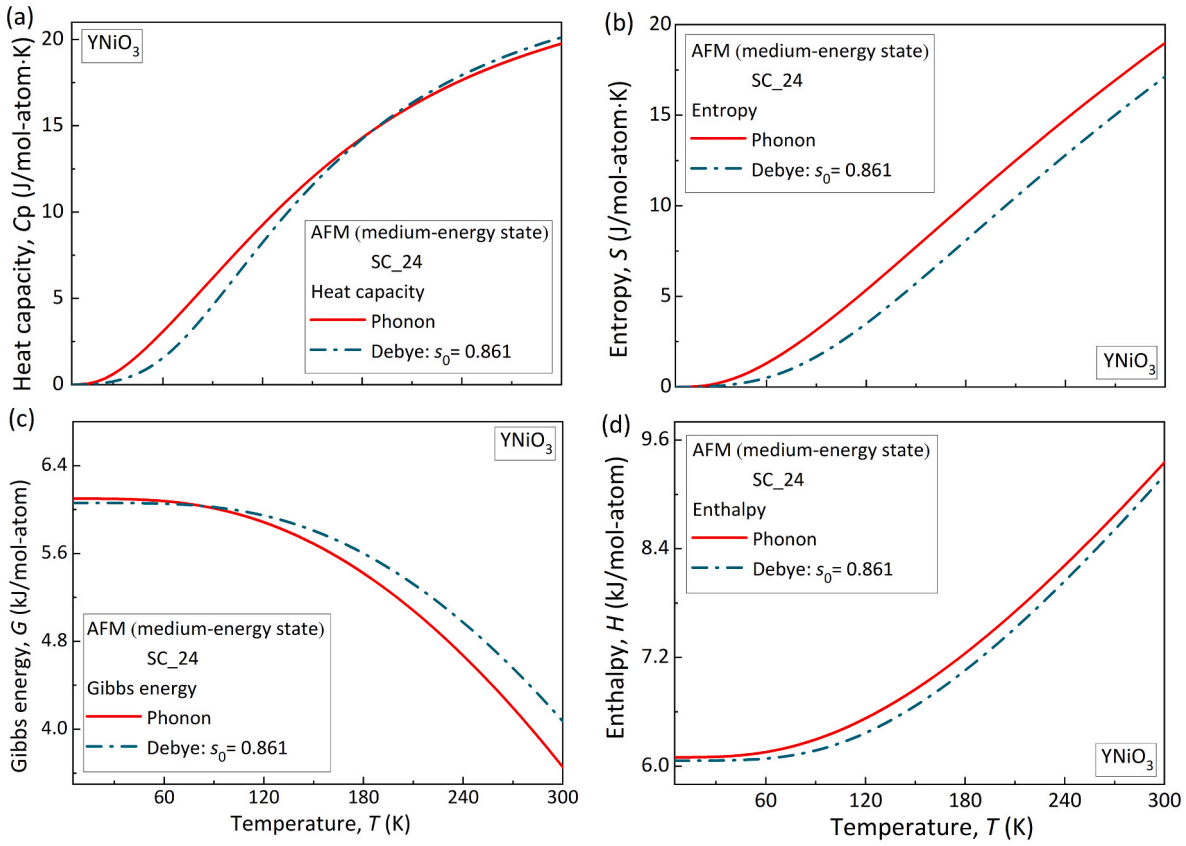

Fig. A6. Calculated configuration-dependent thermodynamic quantities at finite temperature of the spin configuration above the spin ground state (SC_24 with medium energy) for the monoclinic $P2_1/n$ $YNiO_3$ obtained by the DFT phonon calculations and the Debye model, including (a) Heat capacity *C*p, (b) Entropy *S*, (c) Gibbs energy *G*, and (d) Enthalpy *H*. The results based on the DFT phonon calculations are denoted by the red solid line, and those based on the Debye model with scaling factor of $s_0 = 0.861$ adjusted using phonon data by the green dash line.

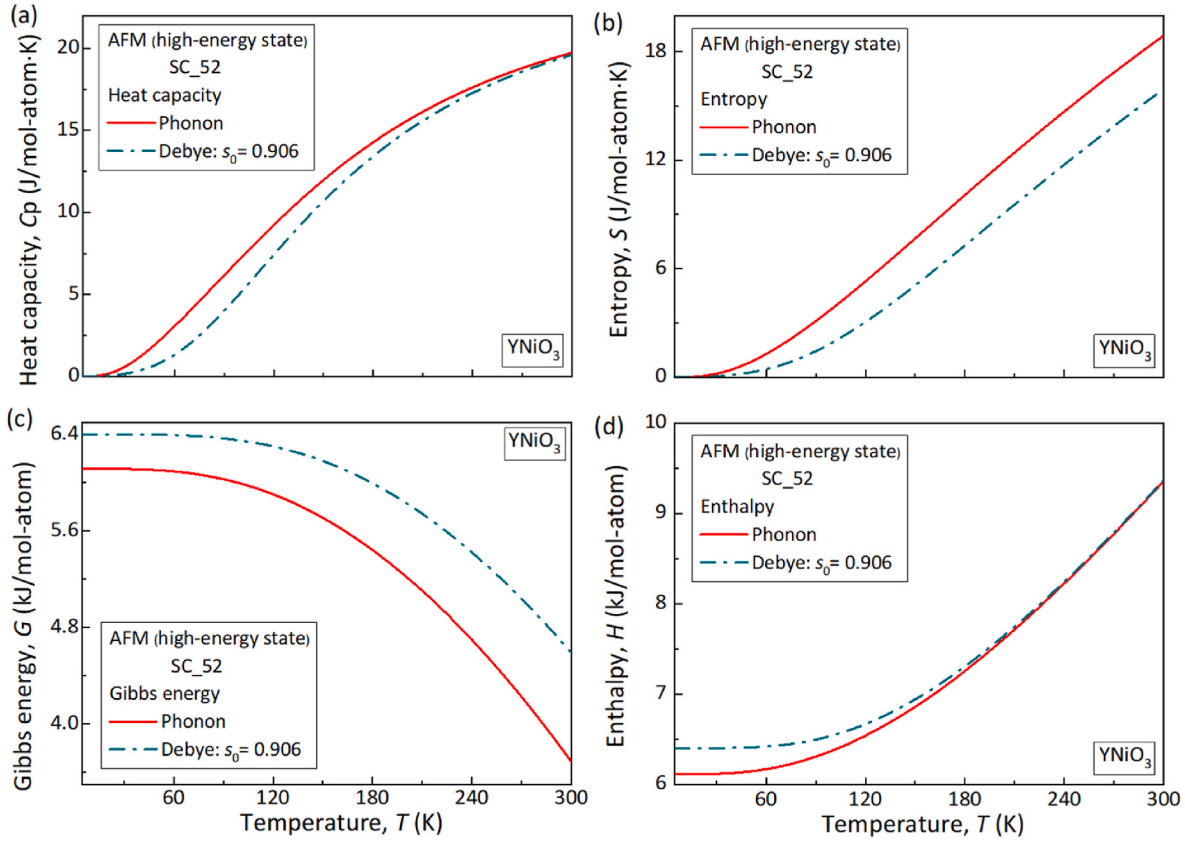

Fig. A7. Calculated configuration-dependent thermodynamic quantities at finite temperature of the spin configuration above the spin ground state (SC_52 with high energy) for the monoclinic $P2_1/n$ $YNiO_3$ obtained by the DFT phonon calculations and the Debye model, including (a) Heat capacity *C*p, (b) Entropy *S*, (c) Gibbs energy *G*, and (d) Enthalpy *H*. The results based on the DFT phonon calculations are denoted by the red solid line, and those based on the Debye model with scaling factor of $s_0 = 0.906$ adjusted using phonon data by the green dash line.

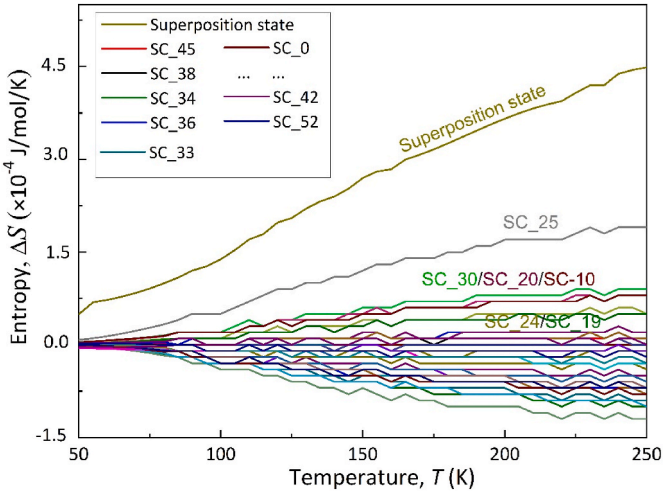

Fig. A8. Calculated configuration-dependent entropy of the 37 independent spin configurations (SC) in the monoclinic $P2_1/n$ $YNiO_3$ system as a function of temperature under the external pressure of P = 0 GPa, where the entropy of the spin ground state AFM configuration is taking as a reference for each case.

References

[1] L.D. Landau, E.M. Lifschitz, Statistical Physics Part 2 Theory of Condensed State, ume 9, Pergamon Press Ltd Headington Hill Hall, Oxford OX3 0BW, England, 1980, pp. 223–310. Course of Thoeretical Physics.

[2] J. Kanamori, Y. Kakehashi, Conditions for the existence of ordered structure in binary alloy systems, J. Phys. Colloq. 38 (1977). C7-274-C7-9.

[3] F. Ducastelle, Order and Phase Stability in Alloys, vol. 114, Springer Series in Solid-State Sciences Springer-Verlag Berlin Heidelberg, 1993, pp. 133–142.

[4] R. Kikuchi, Superposition approximation and natural iteration calculation in cluster-variation method, J. Chem. Phys. 60 (1974) 1071–1080.

[5] D.D. Fontaine, Cluster Approach to order-disorder transformations in alloys, Solid Sate Phy. 47 (1994) 33–176.

[6] A. Zunger, Statics and Dynamics of Alloy Phase Transformations: First-Principles Statistical Mechanics of Semiconductor Alloys and Intermetallic Alloys, vol. 10013, Plenum Press, New York, 1994, pp. 361–419.

[7] G. Trimarchi, Z. Wang, A. Zunger, Polymorphous band structure model of gapping in the antiferromagnetic and paramagnetic phases of the Mott insulators MnO, FeO, CoO, and NiO, Phys. Rev. B 97 (2018).

[8] A.M. Glazer, Simple ways of determining perovskite structures, Acta Crystallogr. A31 (1975) 756–762.

[9] Z. Wang, X.-G. Zhao, R. Koch, S.J.L. Billinge, A. Zunger, Understanding electronic peculiarities in tetragonal FeSe as local structural symmetry breaking, Phys. Rev. B 102 (2020): 235121.

[10] J. Varignon, M. Bibes, A. Zunger, Mott gapping in 3d ABO_3 perovskites without Mott-Hubbard interelectronic repulsion energy, U. Phy. Rev. B. 100 (2019): 035119, 1-8.

[11] J. Varignon, M.N. Grisolia, J. Íñiguez, A. Barthélémy, M. Bibes, Complete phase diagram of rare-earth nickelates from first-principles, npj Quantum Mater. 2 (2017) 1–9.

[12] Y. Zhang, J. Hong, B. Liu, D. Fang, Strain effect on ferroelectric behaviors of $BaTiO_3$ nanowires: a molecular dynamics study, Nanotechnology 21 (2010): 015701.

[13] M. Marathe, C. Ederer, Electrocaloric effect in $BaTiO_3$: a first-principles-based study on the effect of misfit strain, Appl. Phys. Lett. 104 (2014): 212902, 1-3.

[14] M. Paściak, S.E. Boulfelfel, S. Leoni, Polarized cluster dynamics at the paraelectric to ferroelectric phase transition in $BaTiO_3$, J. Phys. Chem. B 114 (2010) 16465–16470.

[15] H. Shi, D. Han, S. Chen, M.-H. Du, Impact of metal ns^2 lone pair on luminescence quantum efficiency in low-dimensional halide perovskites, Phy. Rev. Mater. 3 (2019): 034604, 1-7.

[16] X.-G. Zhao, Zhi Wang, O.I. Malyi, A. Zunger, Effects of static local distortions vs. dynamic motions on the stability and band gaps of cubic oxide and halide perovskites, Mater. Today 49 (2021) 107–122.

[17] O.I. Malyi, A. Zunger, False metals, real insulators, and degenerate gapped metals, Appl. Phys. Rev. 7 (2020): 041310, 1-23.

[18] J.M. Schoen, Augmented-plane-wave virtual-crystal approximation, Phys. Rev. 184 (1969) 858–863.

[19] L. Nordheim, Zur elektronentheorie der Metalle. I, Ann. Phys. 9 (1931) 607–640.

[20] B.L. Gyorffy, Coherent-potential approximation for a nonoverlapping-muffin-tin-potential model of random substitutional alloys, Phys. Rev. B 5 (1972) 2382–2384.

[21] P. Soven, Contribution to the theory of disordered alloys, Phys. Rev. 178 (1969) 1136–1144.

[22] B. Velický, S. Kirkpatrick, H. Ehrenreich, Single-site approximations in the electronic theory of simple binary alloys, Phys. Rev. 175 (1968) 747–766.

[23] A. Zunger, S. Wei, L.G. Ferreira, J.E. Bernard, Special quasi-random structures, Phys. Rev. Lett. 65 (1990) 353–356.

[24] V. Blum, G.L.W. Hart, M.J. Walorski, A. Zunger, Using genetic algorithms to map first-principles results to model Hamiltonians: application to the generalized Ising model for alloys, Phys. Rev. B (2005) 72.

[25] J.W.D. Connolly, A.R. Williams, Density-functional theory applied to phase transformations in transition-metal alloys, Phys. Rev. B 27 (1983) 5169–5172.

[26] J.M. Sanchez, F. Ducastelle, Generalized cluster decription of multicomponent systems, Physica 128A (1984) 334–350.

[27] D.M. Wood, Coherent epitaxy, surface effects, and semiconductor alloy phase diagrams, J. Vac. Sci. Technol. B: Microelectron. Nanometer Structures Proc. , Measur.,Phenomena 10 (1992) 1675–1682.

[28] J. Bréger, M. Jiang, N. Dupré, Y.S. Meng, Y. Shao-Horn, G. Ceder, et al., High-resolution X-ray diffraction, DIFFaX, NMR and first principles study of disorder in the Li_2MnO_3–$Li[Ni_{1/2}Mn_{1/2}]O_2$ solid solution, J. Solid State Chem. 178 (2005) 2575–2585.

[29] S.P. Ong, L. Wang, B. Kang, G. Ceder, Li-Fe-P-O2 phase diagram from first principles calculations, Chem. Mater. 20 (2008) 1798–1807.

[30] A.I. Liechtenstein, M.I. Katsnelson, V.P. Antropov, V.A. Gubanov, Local spin density functional approach to the theory of exchange interactions in ferromagnetic metals and alloys, J. Magn. Magn Mater. 67 (1987) 65–74.

[31] A. Franceschetti, S.V. Dudiy, S.V. Barabash, A. Zunger, J. Xu, M. van Schilfgaarde, First-principles combinatorial design of transition temperatures in multicomponent systems: the case of Mn in GaAs, Phys. Rev. Lett. 97 (2006): 047202.

[32] I.A. Abrikosov, A.E. Kissavos, F. Liot, B. Alling, S.I. Simak, O. Peil, et al., Competition between magnetic structures in the Fe rich fcc FeNi alloys, Phys. Rev. B 76 (2007).

[33] D. Gambino, B. Alling, Lattice relaxations in disordered Fe-based materials in the paramagnetic state from first principles, Phys. Rev. B 98 (2018).

[34] D. Gambino, M. Arale Brännvall, A. Ehn, Y. Hedström, B. Alling, Longitudinal spin fluctuations in bcc and liquid Fe at high temperature and pressure calculated with a supercell approach, Phys. Rev. B 102 (2020).

[35] W. Zhong, D. Vanderbilt, K.M. Rabe, First-principles theory of ferroelectric phase transitions for perovskites: the case of $BaTiO_3$, Phys. Rev. B 52 (1995) 6301–6312.

[36] J.B. Neaton, C. Ederer, U.V. Waghmare, N.A. Spaldin, K.M. Rabe, First-principles study of spontaneous polarization in multiferroic $BiFeO_3$, Phys. Rev. B 71 (2005).

[37] R.D. King-Smith, D. Vanderbilt, First-principles investigation of ferroelectricity in perovskite compounds, Phys. Rev. B 49 (1994) 5828–5844.

[38] L.G. Ferreira, S.H. Wei, A. Zunger, First-principles calculation of alloy phase diagrams: the renormalized-interaction approach, Phys. Rev. B 40 (1989) 3197–3231.

[39] Y. Wang, L.G. Hector, H. Zhang, S.L. Shang, L.Q. Chen, Z.K. Liu, Thermodynamics of the Ce γ–α transition: density-functional study, Phys. Rev. B 78 (2008).

[40] F. Körmann, A. Dick, B. Grabowski, B. Hallstedt, T. Hickel, J. Neugebauer, Free energy of bcc iron: integratedab initioderivation of vibrational, electronic, and magnetic contributions, Phys. Rev. B 78 (2008).

[41] A. Schleife, C. Rödl, J. Furthmüller, F. Bechstedt, Electronic and optical properties of $Mg_xZn_{1-x}O$ and $Cd_xZn_{1-x}O$ fromab initiocalculations, New J. Phys. 13 (2011): 085012, 1-24.

[42] S. Catalano, M. Gibert, J. Fowlie, J. Iniguez, J.M. Triscone, J. Kreisel, Rare-earth nickelates $RNiO_3$: thin films and heterostructures, Rep. Prog. Phys. 81 (2018): 046501.

[43] M.L. Medarde, Structural, magnetic and electronic properties of $RNiO_3$ perovskites (R= rare earth), J. Phys. Condens. Matter 9 (1997) 1679–1707.

[44] J.A. Alonso, J.L. García-Muñoz, M.T. Fernández-Díaz, M.A.G. Aranda, M. J. Martınez-Lope, M.T. Casais, Charge disproportionation in $RNiO_3$ perovskites: simultaneous metal-insulator and structural transition in $YNiO_3$, Phys. Rev. Lett. 82 (1999) 3871–3874.

[45] M.T. Causa, R.D. Sánchez, M. Tovar, J.A. Alonso, M.J. Martínez-Lope, Charge disproportionation in $YNiO_3$: ESR and susceptibility study, Phys. Rev. B 68 (2003): 024429, 1-5.

[46] J.L. García-Muñoz, M. Amboage, M. Hanfland, J.A. Alonso, M.J. Martínez-Lope, R. Mortimer, Pressure-induced melting of charge-order in the self-doped Mott insulator $YNiO_3$, Phys. Rev. B 69 (2004): 094106, 1-6.

[47] C. Piamonteze, H.C.N. Tolentino, A.Y. Ramos, N.E. Massa, J.A. Alonso, M. J. Martínez-Lope, et al., Short-range charge order in $RNiO_3$ perovskites (R= Pr, Nd, Eu, Y) probed by x-ray-absorption spectroscopy, Phys. Rev. B 71 (2005): 012104, 1-4.

[48] A. Alonso, M.J. Martinez, M.T. Casais, M.A.G. Aranda, MTíz Fernández-Diaz, Metal-insulator transitions, structural and microstructural evolution of $RNiO_3$ (R= Sm, Eu, Gd, Dy, Ho, Y) perovskites: evidence for room-temperature charge disproportionation in monoclinic $HoNiO_3$ and $YNiO_3$, J. Am. Chem. Soc. 121 (1999) 4754–4762.

[49] J.A. Alonso, M.J. Martínez-Lope, M.T. Casais, J.L. García-Muñoz, M.T. Fernández-Díaz, M.A.G. Aranda, High-temperature structural evolution of $RNiO_3$ (R= Ho, Y, Er, Lu) perovskites: charge disproportionation and electronic localization, Phys. Rev. B 64 (2001).

[50] M. Medarde, C. Dallera, M. Grioni, B. Delley, F. Vernay, J. Mesot, et al., Charge disproportionation in $RNiO_3$ perovskites (R= rare earth) from high-resolution x-ray absorption spectroscopy, Phys. Rev. B 80 (2009): 245105, 1-5.

[51] H. Park, A.J. Millis, C.A. Marianetti, Site-selective Mott transition in rare-earth-element nickelates, Phys. Rev. Lett. 109 (2012): 156402, 1-5.

[52] H. Park, A.J. Millis, C.A. Marianetti, Total energy calculations using DFT+DMFT: Computing the pressure phase diagram of the rare earth nickelates, Phys. Rev. B 89 (2014): 245133, 1-5.

[53] B. Lau, A.J. Millis, Theory of the magnetic and metal-insulator transitions in $RNiO_3$ bulk and layered structures, Phys. Rev. Lett. 110 (2013): 126404.

[54] S. Middey, J. Chakhalian, P. Mahadevan, J.W. Freeland, A.J. Millis, D.D. Sarma, Physics of ultrathin films and heterostructures of rare-earth nickelates, Annu. Rev. Mater. Res. 46 (2016) 305–334.

[55] J. Varignon, M. Bibes, A. Zunger, Origin of band gaps in 3d perovskite oxides, Nat. Commun. 10 (2019) 1658.

[56] A. van de Walle, Multicomponent multisublattice alloys, nonconfigurational entropy and other additions to the Alloy Theoretic Automated Toolkit, Calphad 33 (2009) 266–278.

[57] J. Du, S.-L. Shang, Y. Wang, A. Zhang, S. Xiong, F. Liu, et al., Underpinned exploration for magnetic structure, lattice dynamics, electronic properties, and disproportionation of yttrium nickelate, AIP Adv. 11 (2021): 015028.

[58] S. Shang, Y. Wang, D. Kim, Z.-K. Liu, First-principles thermodynamics from phonon and Debye model: application to Ni and Ni_3Al, Comput. Mater. Sci. 7 (2010) 1040–1048.

[59] Y. Wang, Z.-K. Liu, L.-Q. Chen, Thermodynamic properties of Al, Ni, NiAl, and Ni_3Al from first-principles calculations, Acta Mater. 52 (2004) 2665–2671.

[60] A. Mercy, J. Bieder, J. Iniguez, P. Ghosez, Structurally triggered metal-insulator transition in rare-earth nickelates, Nat. Commun. 8 (2017) 1677.

[61] E.B. Jones, V. Stevanović, The glassy solid as a statistical ensemble of crystalline microstates, npj Comput. Mater. 6 (2020).

[62] M. Hillert, Phase Equilibria, Phase Diagrams and Phase Transformations Their Thermodynamic Basis, Cambridge University Press, 2008, pp. 1–499. Second.

[63] Y. Wang, S.L. Shang, H. Zhang, L.Q. Chen, Z.K. Liu, Thermodynamic fluctuations in magnetic states: Fe_3Pt as a prototype, Phil. Mag. Lett. 90 (2010) 851–859.

[64] J.P. Perdew, K. Burke, M. Ernzerhof, Generalized gradient approximation made simple, Phys. Rev. Lett. 77 (1996) 3865–3868.

[65] M. Schuler, O.E. Peil, G.J. Kraberger, R. Pordzik, M. Marsman, G. Kresse, et al., Charge self-consistent many-body corrections using optimized projected localized orbitals, J. Phys. Condens. Matter 30 (2018): 475901.

[66] P.E. Blochl, O. Jepsen, O.K. Andersen, Improved tetrahedron method for Brillouin-zone integrations, Phys. Rev. B 49 (1994) 16223–16233.

[67] M. Gajdoš, K. Hummer, G. Kresse, J. Furthmüller, F. Bechstedt, Linear optical properties in the projector-augmented wave methodology, Phys. Rev. B 73 (2006).

[68] S.L. Dudarev, G.A. Botton, S.Y. Savrasov, C.J. Humphreys, A.P. Sutton, Electron-energy-loss spectra and the structural stability of nickel oxide: an LSDA+U study, Phys. Rev. B 57 (1998) 1505–1509.

[69] A. Dal Corso, Projector augmented-wave method: application to relativistic spin-density functional theory, Phys. Rev. B 82 (2010): 075116, 1-18.

[70] Y. Wang, J.J. Wang, W.Y. Wang, Z.G. Mei, S.L. Shang, L.Q. Chen, et al., A mixed-space approach to first-principles calculations of phonon frequencies for polar materials, J. Phys. Condens. Matter 22 (2010): 202201.

[71] Y. Wang, L.-Q. Chen, Z.-K. Liu, YPHON: a package for calculating phonons of polar materials, Comput. Phys. Commun. 185 (2014) 2950–2968.

[72] M.A. Blanco, E. Francisco, V. Luaña, GIBBS: isothermal-isobaric thermodynamics of solids from energy curves using a quasi-harmonic Debye model, Comput. Phys. Commun. 158 (2004) 57–72.

[73] G. Demazeau, A. Marbeuf, M. Pouchard, P. Hagenmuller, Sur uue S&e de ComposCs Oxygknes du Nickel Trivalent Derivis de la Perovskite, J. Solid State Chem. 3 (1971) 582–589.

[74] J.S. Zhou, J.B. Goodenough, B. Dabrowski, Exchange interaction in the insulating phase of $RNiO_3$, Phys. Rev. Lett. 95 (2005): 127204.

[75] A. Zunger, O.I. Malyi, Understanding doping of quantum materials, Chem. Rev. 121 (2021) 3031–3060.
[76] N.F. Mott, Z. Zinamon, The metal-nonmetal transition, Rep. Prog. Phys. 33 (1970) 881–940.
[77] X. Ren, I. Leonov, G. Keller, M. Kollar, I. Nekrasov, D. Vollhardt, LDA+DMFT computation of the electronic spectrum of NiO, Phys. Rev. B 74 (2006).
[78] Y. Shinohara, S. Sharma, S. Shallcross, N.N. Lathiotakis, E.K. Gross, Spectrum for nonmagnetic mott insulators from power functional within reduced density matrix functional theory, J. Chem. Theor. Comput. 11 (2015) 4895–4899.
[79] J. Kuneš, V.I. Anisimov, A.V. Lukoyanov, D. Vollhardt, Local correlations and hole doping in NiO: a dynamical mean-field study, Phys. Rev. B 75 (2007).
[80] S. Biermann, A. Poteryaev, A.I. Lichtenstein, A. Georges, Dynamical singlets and correlation-assisted Peierls transition in VO_2, Phys. Rev. Lett. 94 (2005): 026404.
[81] S.-L. Shang, Y. Wang, Z.-K. Liu, Thermodynamic fluctuations between magnetic states from first-principles phonon calculations: the case of bcc Fe, Phys. Rev. B 82 (2010): 014425, 1-7.
[82] V. Rao Manga, J.E. Saal, Y. Wang, V.H. Crespi, Z.K. Liu, Magnetic perturbation and associated energies of the antiphase boundaries in ordered Ni_3Al, J. Appl. Phys. 108 (2010): 103509, 1-7.